Experimental and numerical study of structural damping in a beam with bolted splice connection

O. Mijatović[1,2], A. Borković[1,3], M. Guzijan-Dilber[4], Z. Mišković[2], R. Salatić[2], R. Mandić[2], and V. Golubović-Bugarski[5]

[1] *University of Banja Luka, Faculty of Architecture, Civil Engineering and Geodesy, Department of Mechanics and Theory of Structures, Bulevar vojvode Stepe Stepanovića 77/3, 78000 Banja Luka, Bosnia and Herzegovina*

[2] *Faculty of Civil Engineering, University of Belgrade, Bulevar kralja Aleksandra 73, 11000 Belgrade, Serbia*

[3] *Institute of Applied Mechanics, Graz University of Technology, Technikerstraße 4/II, 8010 Graz, Austria, aleksandar.borkovic@aggf.unibl.org, aborkovic@tugraz.at*

[4] *Peter the Great St. Petersburg Polytechnic University, Polytechnicheskaya 29, 195251, St. Petersburg, Russia*

[5] *University of Banja Luka, Faculty of Mechanical Engineering, Bulevar vojvode Stepe Stepanovića 71, 78000 Banja Luka, Bosnia and Herzegovina*

Abstract

The objective of this research is to develop a numerical model of one widely used bolted beam splice connection that dissipates energy through the structural damping. The reference experimental setup is carefully designed such that the highly nonlinear dynamic response due to the suddenly released load is obtained. The fact that the monolithic beam with welded connection has a linear response is utilized for the initial calibration of the numerical and experimental models. Then, the numerical model of bolted beam splice connection is verified and adopted through an iterative process. The influences of time and spatial integration, bolt load application, element type, contact formulation, bulk viscosity, and mass scaling are discussed. A special attention is given to the load application and load release functions. After the verification, the Abaqus/Explicit numerical model is validated through the comparison with experimental data, where an appropriate friction coefficient is adopted. It is demonstrated that the nonlinear structural damping occurs due to the complex micro slip behavior at the contact interface.

Keywords: bolted beam splice connection; nonlinear dynamic analysis; structural damping; frictional contact;

1 Introduction

The design of modern steel and aluminum structures requires various mechanical connections. One of the most prominent types of these mechanical joints is the bolted splice

connection (BSC), designed by introducing a large compression force between the elements in contact interaction. The basic function of a BSC is to connect two elements and to allow the force transfer between them. The mechanical behavior of these joints plays an important role in the overall dynamic response of complex engineering structures. Eigenmodes of vibration and nonlinear structural response heavily depend on contact interactions in BSCs. For example, the stress distribution and slip/stick phenomena in joints can affect the stiffness, plasticity, and frictional damping [1]. Therefore, a great amount of research is dedicated to the development of accurate, general, and efficient computational and experimental models of structures with mechanical connections and interfaces [2, 3].

Different types of mechanical connections are displayed in Fig. 1. The connection

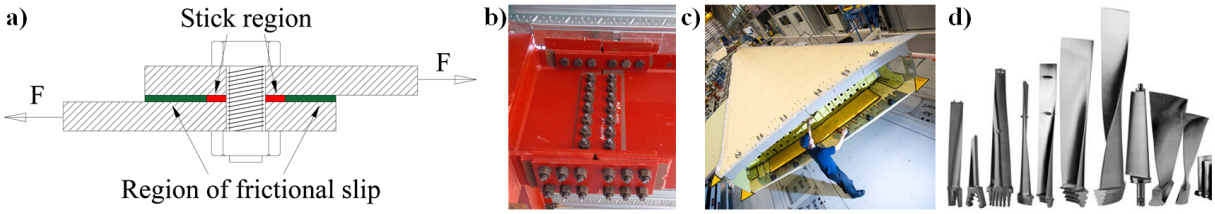

Figure 1: Typical mechanical connections: a) the simple overlap connection with stick and slip regions, b) the bolted beam splice connection in steel structures, c) the splice connection in the aviation industry [4], d) turbine blades with fir-tree connections [5].

shown in Fig. 1a represents a basic scheme of the BSC with its stick and slip regions. Fig. 1b shows a bolted beam splice connection (BBSC), which is one of the most common connections in structural engineering. Furthermore, the various BSCs that are predominantly used in the aviation industry are displayed in Fig. 1c. The fir-tree connections between turbine blades and the mounting disc are shown in Fig. 1d. They require special attention due to the complexity of the wear, damage, and energy dissipation processes [6, 7].

The standard numerical approach for the analysis and design of mechanical connections is the finite element (FE) method [8–10]. It can estimate eigenmodes and system response, therefore allowing the design with respect to a given criterion and material properties. One of the remaining challenges is to implement uncertainties of geometric and material properties of the BSC contact interactions in the FE codes. This means that the problem of accurate and efficient modeling of BSCs during the nonlinear dynamic response still open. The main issue is the modeling of structural damping, which is the prevailing mechanism of energy dissipation in jointed structures. Structural damping strongly affects the dynamic response and eigenmodes, making the problem of jointed structures highly nonlinear. Despite its utmost importance, this phenomenon is yet to be well-understood.

Structural damping of jointed structures largely depends on the properties of surfaces in contact interactions and on the activation of stick/slip regions during the dynamic response. A well-designed bolted connection prevents macro slip and a part of micro slips, but some micro-slipping is always present in real-life working conditions [2, 3]. In other words, during the motion of a structure, the small regions of contact interface will move relative to each other, while the majority of contact interface will stay fixed with respect to each other. The areas where these states exist are defined as the slip and

the stick regions, respectively. It is evident that the stick region will appear below and in the close area around the bolt head, see Fig. 1a. Let us emphasize again that, on a macro level, the parts of a well-designed joint should not move with respect to each other. The mentioned relative motion occurs over small regions of the interface area and it is designated as the micro slip. As the intensity of excitation force increases, the micro slip region increases as well. If the excitation exceeds a threshold value, the entire contact interface slips, and this phenomenon is designated as the macro slip [11–13].

The lack of proper understanding of jointed structures is discussed by Segelman [2]. Twenty researches were asked: "What are the modeling approaches in which you define and model mechanical connections?" It was found that there were more ways to describe mechanical connections than there were survey participants. Hence, there is no uniform solution or agreement when it comes to the computational modeling of mechanical connections and structural damping.

Let us briefly discuss some of the main factors that influence contact interaction. The problem is more complex than the pure friction described by Coulomb's law and the friction coefficient [14–16]. Additional parameters are material change, plastification, and degradation [16, 17]. These are followed by unpredictable changes in the total real contact area involved in the interaction [18] and by changes in stick/slip conditions [19, 20]. Another important property is the surface roughness, which is crucial for some engineering applications. For the definition of contact geometry, Greenwood-Williamson's and Persson's models are readily used [21–23]. Contact geometry and the separation are highly nonlinear and their numerical solution requires a massive computational algorithm [24, 25]. Therefore, accurate modeling of contact geometry is a challenging task, either with experimental, analytical, or numerical approaches [16, 17, 19, 20, 26–32]. The complexity of contact modeling increases with a decrease in scale while gaining further insight into its real nature. The contact interaction of two general bodies at an atomic or nano-level is a multi-physical problem where several scientific disciplines intertwine [33].

It is fascinating that practically all surfaces found in nature have roughness, with the exception of some unique materials such as mica, which has a smooth molecular surface [34]. The influence that contact surface roughness, as a micro scale quantity, has on the overall macro response of a bolted connection is investigated by Segalman and Brake [2, 3, 35]. In these studies, the authors emphasize the contact roughness influence on the jointed structure response and contact pressure distribution. Furthermore, the dry friction between two stainless steel wedges with a contact interaction surface of only 1 mm^2 was examined by Fantetti et al. [36]. Despite the extremely small contact area, the roughness change in contact surfaces due to the sliding friction caused a significant change in the eigenmodes of the complete experimental setup that had weight of 22.4 kg! This experiment clearly indicates the substantial influence that roughness has on dynamic response.

When we limit the research to dry friction and aim to compare numerical and experimental results, we should consider what dry friction actually is, and whether and in what way it is possible to achieve ideally dry and clean metal surfaces without the influences of oxides and humidity [17, 37, 38]. It is remarkable that even an apparently trivial phenomenon, such as air humidity, can significantly affect the friction in joints [39, 40] and thus, structural damping. Also, oxides and their formation time considerably influence the friction in mechanical connections [16, 17, 41]. The physical and mechanical characteristics of the oxide and its effect on the friction and overall response of the jointed

structures are yet to be fully understood [17, 42]. Various experimental procedures have shown that, after the oxide thickness exceeds the limit of $5 - 10\ nm$, the friction between steel surfaces reduces due to adhesion reduction [43–45]. For very clean smooth surfaces and tests performed in a vacuum immediately after cleaning, it has been found that the friction can increase by several orders of magnitude [41, 46–48]. Furthermore, during the high frequency micro- and macro-slipping under large pressure, the micro asperities yield and melt, which requires a proper thermodynamical formulation and further complicates the dry friction contact modeling. A process of the local heating and melting of micro asperities is known as *flash-heating*, and it reduces friction [49–51].

Besides the aforementioned phenomena that are mostly related to dry friction, let us note additional parameters that affect friction in general: type of material [52–54], lubrication and presence of different fluids [55–57], and changes in the material phase and structure caused by heating or radiation [58]. Again, this brief review of the main parameters that affect contact interactions reveals why the modeling of connections in engineering structures is an active and challenging research area. In essence, the impact that processes at the nano and atomic levels have on the macro scale system response perplexes the accuracy and efficiency of mechanical models [34, 59].

To sum up, there are three main approaches to the study of joint dynamics. The first approach is to define the exact physics of an interaction of the bolted connection starting from the micro scale and to consider a variety of uncertainties related to the description of surfaces that come into contact. The second approach is to investigate the joint dynamics at the macro scale, thus avoiding the description of micro scale surface geometry and the conditions of contacting parts. The objective of this approach is to investigate the dynamic response of the joint as a whole, and to identify crucial parameters that allow the prediction of structural response. Finally, there is a multi-scale approach that acquires data from the micro scale and applies it via appropriate parameters to the macro scale models.

Different experimental and numerical models for joint dynamics at the macro scale exist [13, 60–65]. Most of these approaches are based on detailed experimental and numerical analyses of simple models. For such models, implicit numerical procedures do not suffer from convergence issues and can provide satisfactory results. A detailed insight into the nonlinear response of bolted joints is accomplished through a series of experiments and by the development of a numerical procedure using a four-parameter Iwan model [2, 3, 66–70]. The importance of scaling between the bolt tightening force and the excitation force magnitude is observed in these experiments. In the case when the disturbing force magnitude is small in relation to the bolt tightening force, the connection will not be activated. In other words, the size of the micro slip regions inside the contact interaction will not reach a threshold value that triggers the nonlinear dynamic response, i.e. structural damping. If this is the case, the majority of the contact interaction is in the stick regime and only material damping will occur. For simple steel structures, such as beams and brackets, the material damping ratio is around 0.001 [2, 3, 63].

This brief review shows that contact in structural connections is a phenomenon that requires further investigation. The issues relating to the contact between two bodies and the description of a process that takes place within the interaction of their contact surfaces can be classified as an exceedingly nonlinear dynamic problem for which no single and uniform solution exists [2, 3, 24, 71, 72]. Therefore, the papers dealing with the structural damping in BBSCs are rare in the literature. The presented research is based

on a macro scale approach and the secondary phenomena arising in bolted connections that can significantly influence structural dynamic response.

Motivated by the complexity of contact interactions and their importance for engineering structures, one mechanical joint is studied in detail. Some preliminary findings are already discussed in [73, 74]. The main contributions of the presented research are the comprehensive calibration, verification, and validation of a numerical model of one BBSC. The experiment was carefully designed to trigger a significant nonlinear dynamic response of an IPE cantilever beam. For the initial verification, a model with welded connection was utilized. Then, by a deliberate calibration of the numerical model using Abaqus/Explicit, we obtained a reasonably accurate nonlinear structural response. The adopted BBSC numerical model allows an insight into the complex stick/slip state, which is the main cause of structural damping. The Abaqus model has 69 contact pairs, which presents a complicated problem from the point of view of contact mechanics. Yet, from the point of view of structural engineering, this joint is a simple and widely used connection. To bridge this gap, the main issue is the balance between the accuracy and efficiency of available formulations and tools. For numerical simulations, we utilized several different computer configurations. For reference, the presented computational times are given for the configuration with i7-9700K CPU and 32GB RAM.

The paper is organized as follows. The next section presents the experimental setup, results, and post-processing procedure. The calibration, verification and validation of the numerical model are given in Section 3. The main findings and conclusions are discussed in the last section.

2 Experimental analysis

The experimental analysis consists of three steps: (i) design, preparation, and realization of the experimental testing, (ii) processing of the obtained data, and (iii) analysis of the results. These steps are discussed in detail in this section. In addition to the experimental model, an outlook towards the numerical model and its results is given. This kind of presentation is practically unavoidable since both numerical and experimental analyses are intertwined.

2.1 Experimental setup

To enable a consistent comparison of the experimental and numerical results, it was necessary to properly define the experimental setup. This includes the design of connections and load, definition of the loading procedure, and design of the clamped boundary condition.

2.1.1 General considerations

The aim of the experimental analysis was to examine the nonlinear behavior caused by a sudden release of the load of one commonly utilized IPE 80 beam with a BBSC in real-life working conditions. Therefore, the experiment ws set up in the open, with relative air humidity of approximately 70-80%. Besides the BBSC, a model with a welded beam splice connection (WBSC) was considered as well. Since the WBSC is monolithic, it is sensible to assume that this beam will oscillate within the linear range. This behavior

makes the WBSC model ideally suited for the calculation of the material damping and the initial calibration of the numerical model.

A detailed drawing and an image of the physical model are given in Fig. 2. At the free

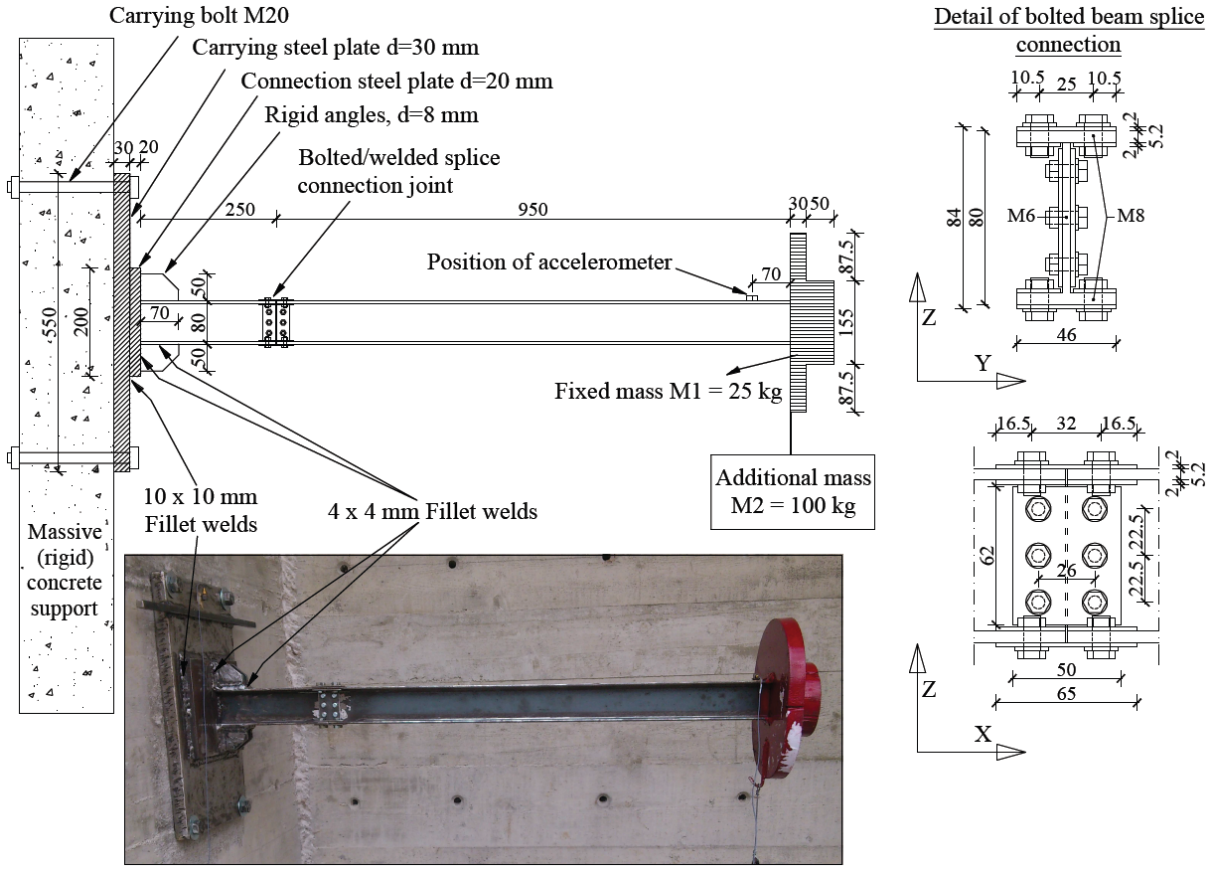

Figure 2: Experimental setup. Detailed drawing and physical model.

end, the beam has a fixed mass (M1) and an additional mass (M2). After a sudden removal of the additional mass, the beam enters the free vibration response. This additional mass is added monotonically by slowly increasing it in increments of 25 kg. The additional mass is then released by cutting the attached wire that is 3 mm thick. In order to reduce the effect of wire cutting on the consistency of the experimental results, we also tested wires that are 1.5 mm and 2 mm thick. However, the 3 mm wire was the thinnest one that could carry the additional mass. The 3 mm wire was near the yield point,so only a small amount of damage was required for it to break. This approach is similar to the modeling of a suddenly released load by Pagnini in [75], where a specially designed test tube was calibrated to break after the load reaches the desired value.

The structural response was measured with a one-axis accelerometer fixed near the free end, see Fig. 2. The accelerometer had a sensitivity of 96.6 mV/g and a frequency range of 0.3–6000 Hz. The sampling rate was set at 128 outputs per second, which was sufficient to capture the considered acceleration response.

2.1.2 Design of clamped boundary condition

One of the most important initial challenges was the design and construction of the clamped boundary condition. Failing to properly build the clamped end could result in

parasitic vibrations due to the rotation of connection plates. Although the final numerical model is defined later in Section 3, we had to consider an initial numerical model to design the physical clamped condition.

Therefore, the aim of the initial numerical analysis was to define a beam model with the clamped boundary condition that can be physically constructed. For comparison, a beam with an ideally defined fixed boundary condition at the end section had been used, Fig. 3.

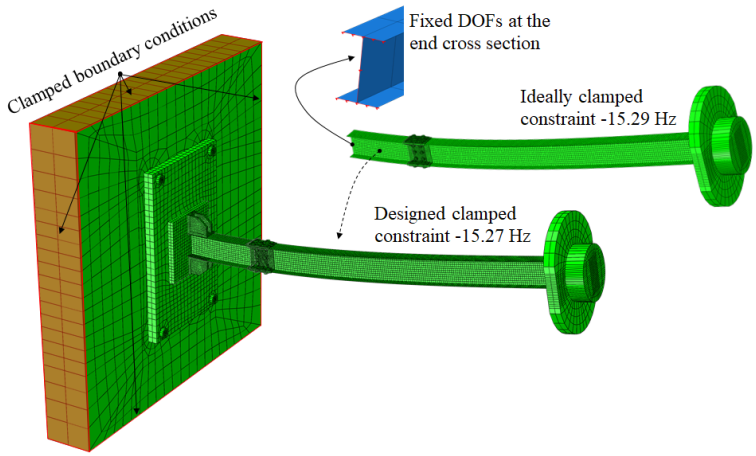

Figure 3: Initial numerical models. Beams with ideal and designed clamped constraints.

The main requirement for the calibration of the model with the designed clamped end was the agreement between the fundamental frequencies of these two models. Concretely, we are observing the lowest bending eigenfrequency with respect to the major axis of inertia. It is actually the third eigenmode of this beam that was the dominantly excited one in our study. The eigenfrequency of the ideally clamped model is 15.29 Hz.

To define a numerical model that can be constructed, several approaches and parameters were considered and varied. The end results are the numerical model in Fig. 3 and the appropriate physical model in Fig. 2. The eigenfrequency of this numerical model with a structurally designed clamped end is 15.27 Hz. The correspondence obtained between the results gave us clearance to continue with the construction of the physical model.

The beam was welded to a $200 \times 200 \times 20$ mm connection steel plate via rigid angles and 4×4 mm welds, Fig. 2. This assembly was then welded to a carrying steel plate with dimensions $550 \times 350 \times 30$ mm. An approximate weld size between the connection and carrying steel plates was 10×10 mm. The use of oversized steel plates and welds was intentional, as it ensured an absolutely rigid connection between the beam and the carrying plate. Finally, the carrying plate was connected to a 300 mm thick concrete wall with four M20 bolts, as shown in Figs. 2 and 3. With such a construction, we have achieved an almost ideal clamped boundary condition.

2.1.3 Model with the bolted beam splice connection

As discussed in the introduction, it is crucial to ensure the activation of micro slip regions in the connection to obtain the nonlinear response of the BBSC. Furthermore, to guarantee consistent results over all tested models, a macro slip had to be allowed during

the application of the load. These requirements are achieved by means of careful design of the connection with respect to the applied load.

The position of the connection was set at 250 mm from the clamped end. To simulate real-life conditions, the static loading due to the masses M1 and M2 was designed to utilize 50 % of the elastic moment capacity of the observed section [76, 77]. Since the BBSC model had been analyzed only with respect to the major principal axis, the required mass was adopted as 125 kg, of which the fixed mass was M1 = 25 kg and the additional M2 = 100 kg.

After defining the static loading, the BBSC was designed, see Figs. 2 and Fig. 4. The

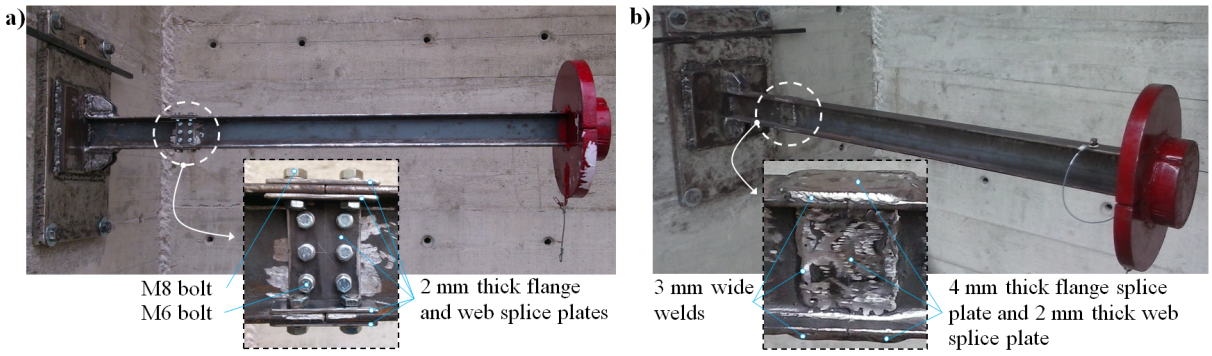

Figure 4: Experimental setup. Images of connections in physical models. a) Bolted beam splice connection. b) Welded beam splice connection.

connection consisted of two $65 \times 46 \times 2$ mm outer flange splice plates and two pairs of $65 \times 18 \times 2$ mm inner flange splice plates. Additionally, the web splice plates were $62 \times 50 \times 2$ mm. The tightening was achieved by four M8 bolts for the flanges and six M6 bolts for the webs. The grade of utilized bolts was 8.8, while the diameters of bolt holes were 10 mm and 8 mm for M8 and M6 bolts, respectively. The holes were designed to provide a 1 mm gap around the bolt's shank. Also, a 1 mm gap was left between the two parts of the beam that had been joined.

The BBSC model was tested at three levels of the bolt tightening force. The values of $M_r = 25\ Nm$ and $M_r = 10\ Nm$ were adopted as the maximum tightening torques for the M8 and M6 bolts, respectively. These torques resulted in respective tightening forces of $F_p = 16\,kN$ and $F_p = 8\,kN$ [78, 79], Table 1. The considered levels of bolt tightening

Table 1: Approximate values of the bolt tightening forces for the three BBSC models.

Model	Tightening force M8 [kN]	Tightening force M6 [kN]	Percentage of maximum force [%]
BBSC100	16	8	100
BBSC50	8	4	50
BBSC30	5	2.5	30

forces were measured with respect to these maximum values. The appropriate models were designated as BBSC100, BBSC50, and BBSC30, and they refer to 100 %, 50 %, and 30 % of the respective maximum tightening force.

With such a design, the requirements for the nonlinear response and the consistent results across different models were satisfied. The macro slip had been anticipated during

the quasi-static application of the additional mass, and the micro slip during the free vibration response. Furthermore, due to the macro-slipping, a complex stress state emerged at the connection. We will discuss this issue further in Subsection 3.4.2 and Section 4.

2.1.4 Model with welded beam splice connection

The WBSC consists of two $65\times45\times4$ mm outer flange splice plates and two $62\times50\times2$ mm web splice plates. Let us note that the two flange splice plates 2 mm thick are applied to the BBSC, while only one flange splice plate 4 mm thick is used for the WBSC. Nevertheless, the moment capacity of both connections is similar if the reduction of the cross-sectional area is neglected due to the bolt holes, Fig. 4.

The bending of the WBSC was examined with respect to both principal axes of inertia. For the loading case with respect to the major principal axis, the masses are the same as for the BBSC: M1 = 25 kg and M2 = 100 kg. Regarding the loading case with respect to the minor principal axis, we have set a requirement that the maximum normal stresses due to the gravity should be close for both loading cases. Since the elastic section moduli with respect to the principal axes of the IPE 80 section are $W_{el,y} = 20.03$ cm^3 and $W_{el,z} = 3.69$ cm^3, the masses M1= 0 kg and M2= 25 kg are adopted for the case of bending with respect to the minor principal axis.

2.2 Experimental results

The experiment was based on the free vibration response approach, during which the acceleration time history was recorded [80]. Then, the auto spectrum response (ASR) was obtained from the recorded accelerations via the Fast Fourier Transform, [81–83]. The advantage of this approach is that a structure can be analyzed in real-life conditions. On the other hand, the free vibration response does not guarantee the excitation of all eigenmodes, in contrast to the experimental modal analysis in controlled conditions using the modal hammer. The number of the recorded modes with the free vibration response depends on the experimental setup, number and positions of accelerometers, load, etc. For the purpose of our analyses, the lowest bending mode in the plane of the load and the beam axis was of the most importance.

As mentioned in Subsection 2.1, the WBSC was tested with respect to both principal axes, and the BBSC only with respect to the major principal axis. The experimental acceleration time histories and the ASRs are presented in this paper, along with the numerical results for the WBSC model.

2.2.1 Model with bolted beam splice connection

The measured acceleration time history responses and ASRs for the models with three different bolt tightening forces are displayed in Figs. 5 and 6. Evidently, the differences in the acceleration amplitudes across the models are significant and the values approximately follow the corresponding tightening force. For example, during the initial 0.5 s, the difference between BBSC100 and BBSC50 is nearly 50%. Next, the difference in amplitudes between BBSC100 and BBSC50 is more pronounced than the difference between BBSC50 and BBSC30. This suggests that the bolts are quite loose for 50%, while for the 30% of the tightening force the connection does not have any slipping resistance left.

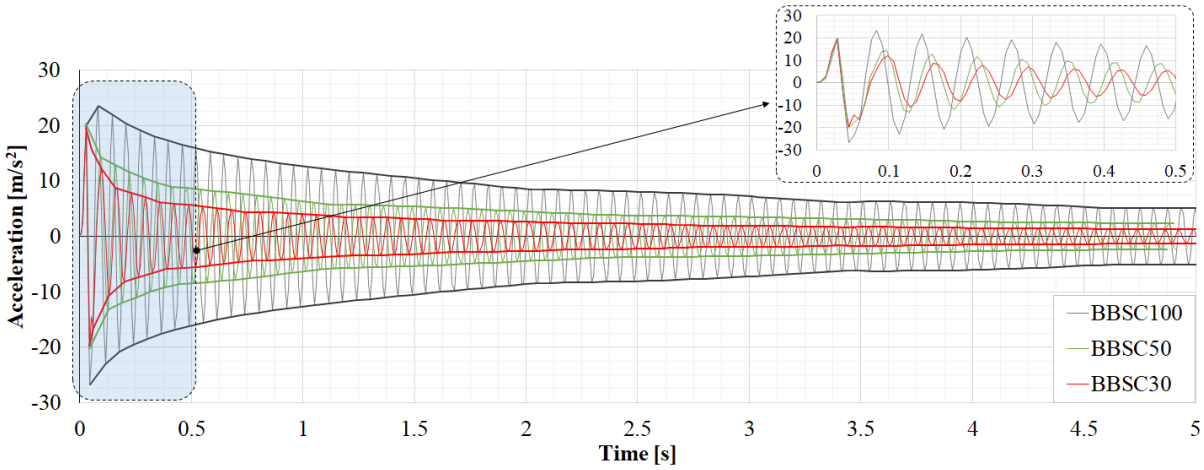

Figure 5: Bolted beam splice connection. Experimental acceleration time histories and their envelopes for the models with three different bolt tightening forces.

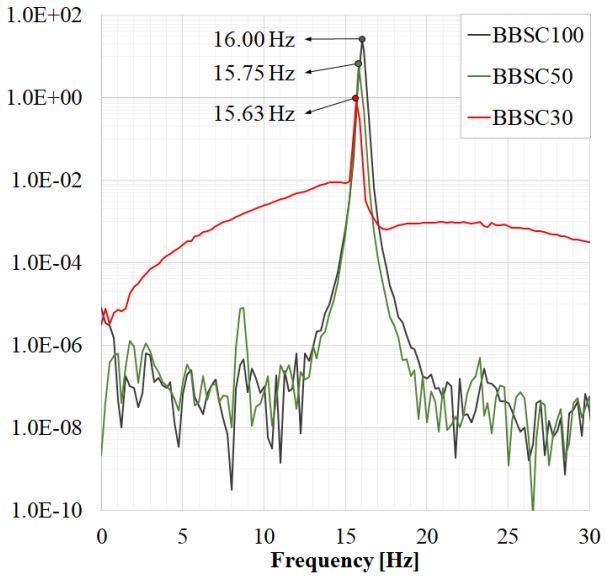

Figure 6: Bolted beam splice connection. Auto spectrum response.

Furthermore, the differences in the periods/frequencies of oscillations are visible and in line with the expectations.

When the full response of 5 s is observed, the beating effect can be noticed. We will discuss this phenomenon thoroughly in Subsection 2.4.1. An important observation is that the first amplitude of acceleration is practically invariant to the value of the tightening force. This fact will be employed to define the load release function of the numerical model in Subsection 3.4.1.

Regarding the ASRs, all three models return similar eigenfrequencies and the differences correspond to the respective bolt tightening forces. As discussed in Subsection 2.1.2, the observed frequency is not the lowest one, but the lowest bending frequency in the plane of the load and the beam axis. Additionally, the ASRs suggest that the damping increases with the reduction of the bolt tightening force.

2.2.2 Model with welded beam splice connection

During the analysis of the WBSC experimental results, a lot of noise was found for the loading case with respect to the major principal axes of inertia. The ASR can be extracted, but the acceleration results were unusable for our analysis and are omitted here. Regarding the loading with respect to the minor principal axis, the acceleration response is shown in Fig. 7. Again, the beating effect is present and it will be discussed later in Subsection 2.4.1.

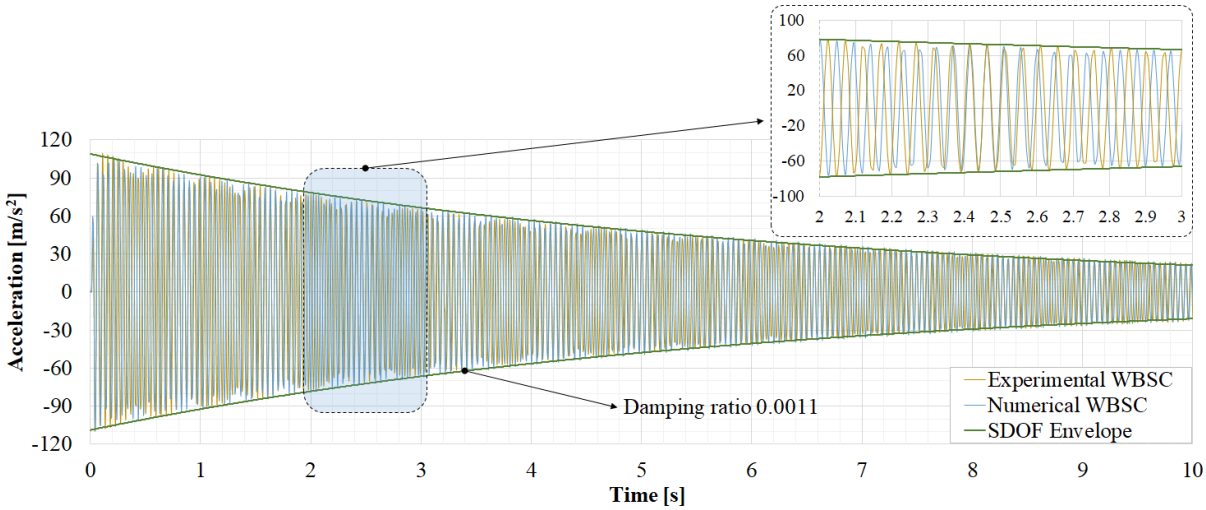

Figure 7: Welded beam splice connection. Experimental and numerical acceleration time histories, and the envelope of a linear single-degree-of-freedom system.

An approximate envelope of amplitudes is plotted on the same graph using the standard exponential law for the amplitude decay of the linear single degree-of-freedom (SDOF) system. Evidently, the acceleration amplitudes are well-described with this envelope. It follows that the WBSC oscillates in a linear range and that it can be approximated with an SDOF. This confirms our assumption from Subsection 2.1.1: the WBSC is practically monolithic and it can dissipate energy only via material damping. This linear response of the WBSC model allows us to estimate the damping ratio that is close to 0.0011, which is in line with the commonly found values of material damping for steel [2, 3, 63].

The adopted numerical model is considered in Section 3. However, for the sake of coherence, some aspects and results of the numerical analysis should be discussed here. First, our adopted numerical model was analyzed using linear modal dynamic analysis and the acceleration response is given in Fig. 7. The numerical and experimental results agree well, which validates the numerical model. This fact allowed us to further calibrate the numerical model and to post-process the experimental results. Second, a lot of noise is detected in the acceleration response during the nonlinear explicit numerical analysis. In order to avoid this issue, the application of filters and high sampling rates would have been required. On the other hand, in comparison with the accelerations, the velocities are significantly less sensitive to sampling rates and high-frequency noise. Hence, the velocity field was referenced almost exclusively in the present research. The calculation of the velocities from the measured acceleration response is discussed in the next subsection.

The ASR responses for the loading with respect to both principal axes are shown in Fig. 8. The lowest eigenfrequency for the case of bending with respect to the major principal axis is smaller than the one with respect to the minor axis, due to their respective

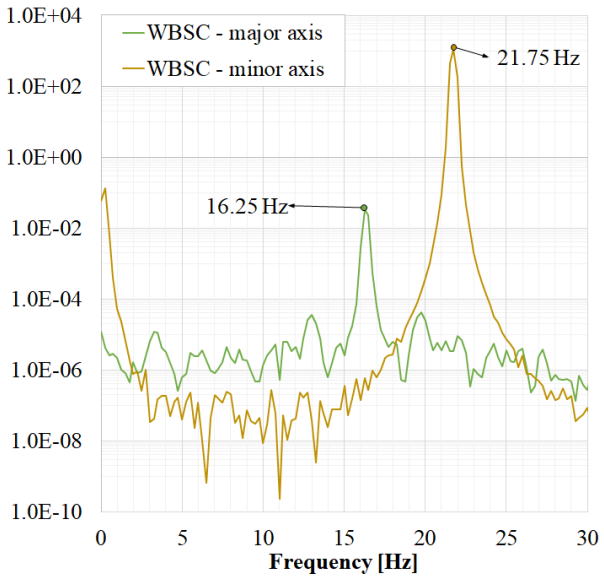

Figure 8: Welded beam splice connection. Auto spectrum responses for two cases of loading.

fixed masses of M1= 25 kg and M1= 0 kg.

2.3 Post-processing of experimental results

2.3.1 Motivation

The low-frequency response is often the focus of structural dynamic simulations. This poses a problem in the numerical analysis when explicit time integration is employed. Namely, the stability requirement of the explicit procedure is that the integration time step should be small enough to capture the highest frequency wave traveling through the mesh. For highly nonlinear problems and fine meshes, this time increment can be extremely small.

When it comes to retrieving the outputs from explicit simulations, the recording of results at every increment produces large output files and has high computational costs. This approach is not optimal when only the low- frequency response is of interest, as in our case. The common solution is to calculate output variables at each n_{out} integration steps or each t_{out} intervals of time. This procedure is needed to optimally utilize computational resources, but can lead to aliasing problems. Aliasing occurs when a signal is sampled at discrete points, but not enough data points are saved to correctly describe the original signal [84, 85]. Different variables have different sensitivities to aliasing. The variables with high frequencies and large amplitudes, such as the accelerations and the reaction forces, are the most susceptible to aliasing [86]. The NASA Technical Memorandum [87] shows that even 10^4 outputs per second are not enough to avoid aliasing in drop test simulations. One way to mitigate aliasing is to use Abaqus real-time filtering capability which requires less disc space than taking output at every increment. This approach has a few drawbacks, such as the choice of an appropriate output rate and filter, which is left at the user's discretion. [88, 89].

Based on these considerations, the outputs in our numerical model were taken every 0.00781 s, which returns the sampling rate of 128 results per second. This rate is the same

as in the experimental analysis, cf. Subsection 2.1.1. The time period considered with numerical analysis was approximately 6.5 s. For the adopted numerical model, Abaqus required approximately 53 h of computational time during which 3×10^7 increments were calculated. To meet the recommendations from [87], the acceleration response needs to be sampled at a 100 times higher rate, which would highly affect computational cost and memory requirements. Our numerical tests confirm that appropriate results can be obtained with 5×10^4 outputs per second for sensitive analysis outputs like the acceleration and the contact forces. To avoid these issues, we have numerically integrated the experimental acceleration responses and obtained velocities that are less sensitive to the low sampling rates. With this approach, we can consistently compare the experimental and numerical data.

2.3.2 Numerical integration of discrete function

Through the numerical integration of a discrete signal, we aim to find the new value v_{i+1} based on the known value v_i. This is achieved by calculating the area under a curve being integrated, between the points i and $i+1$. There are many ways to choose an appropriate integration rule for the integral at hand: One can use the linear interpolation between the points i and $i+1$, and then integrate using the trapezoidal rule, or use spline interpolation through several discrete points in order to decrease the integration step and lower the error. In this work, we have calculated the experimental velocities by approximating the discrete acceleration data with a cubic polynomial, and then integrating it with Simpson's 3/8 rule [90].

In order to validate the described procedure for the calculation of experimental velocities, we first integrated the experimental acceleration response of the WBSC model. It is discussed in Subsections 2.1.1 and 2.2.2 that this model has a linear response and can be used for calibrating the numerical model and the post-processing of the experimental results. Therefore, we have compared these WBSC experimental velocities with the velocities obtained by the modal dynamic procedure in Abaqus. The results agree well and they are omitted for the sake of brevity.

By means of this analysis, the applied cubic numerical integration is validated. The procedure is then utilized to find the velocity time histories of the experimental BBSC models with three levels of bolt tightening force. The results will be shown and discussed later in the paper.

2.4 Approximate calculation of damping

As discussed in Subsection 2.2.2, the WBSC amplitude decay follows an exponential law, meaning that the system response and the damping can be considered linear. By knowing the eigenmodes, the amplitude decay and the energy dissipation of such a system can be described with one parameter - material damping. On the other hand, the BBSC model dissipates energy through a nonlinear mechanism due to the friction between the contacting surfaces. The amplitude decay of such a system cannot, in general, be described with only one parameter.

There is a variety of methods that can be used to identify damping characteristics of a nonlinear system with multiple DOFs. The peak amplitude method is applied for the nonlinear response of shear lap joints in [62]. Damping of structures with bolted connections was considered by Goyder et al. [63, 91, 92]. Their algorithm is based on

fitting the decaying amplitudes along short time intervals using the sine function. Here, we are using an approach similar to the one in [91].

2.4.1 Experimental damping of the beam with welded connection

Since the WBSC model is linear, it is well-suited for the verification of the algorithm for the extraction of damping. Let us assume that the decay rate between two consecutive amplitudes with the same sign is small enough to allow an approximation using the linear oscillator with viscous damping [91]. This is a reasonable assumption for small time increments between amplitudes. Therefore, a discrete set of logarithmic decrements δ_i between two consecutive positive or negative velocity amplitudes was calculated. The damping ratio is then found by the standard expression $\xi_i = \delta_i / \sqrt{4\pi^2 + \delta_i^2}$. In this way, a set of approximate discrete damping ratios is obtained for a complete system response.

Envelopes of the velocity and the calculated discrete damping ratios for the WBSC model are shown in Fig. 9. Due to the presence of beating, the discrete damping ratios

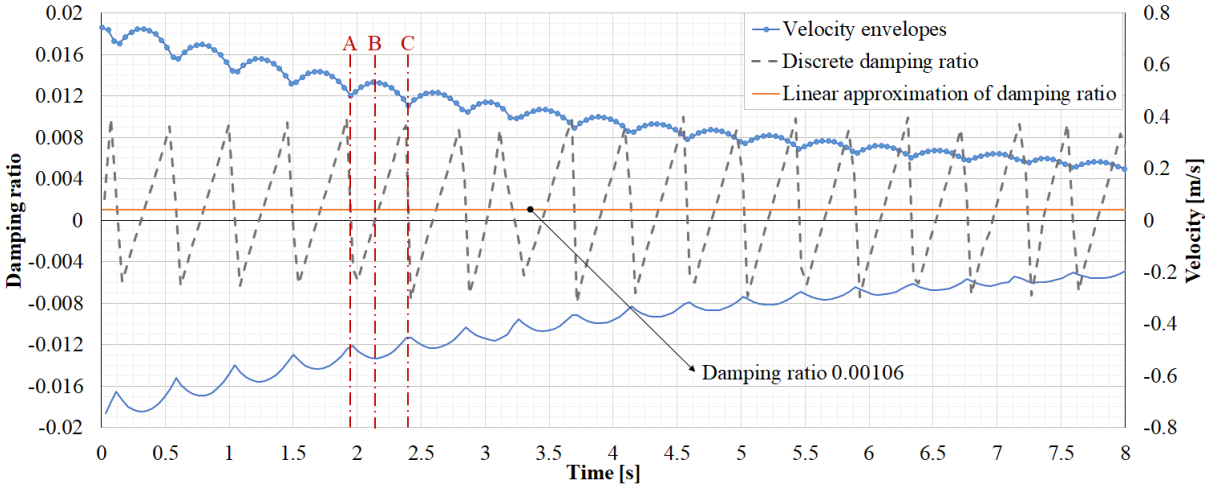

Figure 9: Welded beam splice connection. Velocity amplitudes, discrete damping ratios and linear approximation of damping ratio.

oscillate between positive and negative values. The beating phenomenon occurs when the body oscillates in two different eigenmodes with slightly different frequencies. Manufacturing imperfections, the eccentricity of mass, and similar values of two eigenfrequencies can cause a beam to beat. The beam then oscillates with respect to both of its principal axes and thus in more than one frequency [3]. During such vibrations, the signal appears to be modulated. This is evident in Fig. 9 where the velocity amplitudes decrease, but oscillate in regular intervals. One typical part of the response is marked in Fig. 9 and one period of beating is observed (AC segment). Between points A and B, the nonphysical negative values of the discrete damping ratio occur, because the amplitudes increase in that segment due to beating. Point B is the local maximum of velocity where the discrete damping ratio is zero. The amplitudes decrease in the segment BC and the damping is positive. The discrete damping ratio reaches the maximum just before point C where the beating cycle starts again.

Therefore, due to the beating effect, the discrete damping ratios do not correspond to the true values of damping. This problem is solved by fitting the damping curve

through the discrete set of damping data. Since the WBSC is linear, a simple mean value data fitting is suitable and the result is displayed in Fig. 9. The realistic value of damping is obtained, $\xi = 0.00106$, which agrees with the value calculated using the decaying envelope for the SDOF system with viscous damping, $\xi = 0.0011$, cf. Subsection 2.2.2. This analysis shows that the beating phenomenon has a negligible influence on the damping ratio.

2.4.2 Experimental damping of the beam with bolted connection

As discussed previously, the damping ratio of the BBSC model is not constant during the free vibration response. A straightforward approach for the quasi-viscous approximation of damping is illustrated in Fig. 10 where the velocity amplitude decay for the BBSC100 model is considered. Two envelopes of the linear viscous SDOF system are utilized to

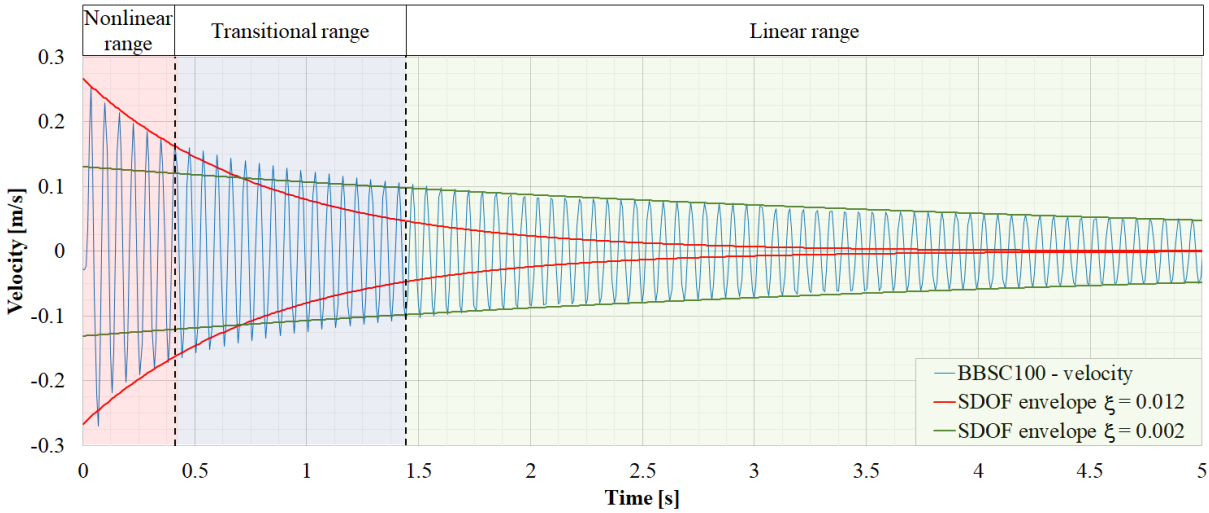

Figure 10: Bolted beam splice connection with 100 % of bolt tightening force. Approximation of damping with two decaying envelopes of the SDOF system.

estimate the damping. The first envelope approximates the energy dissipation during the short initial part of the response for $t < 0.4\ s$ with an approximate damping ratio of $\xi = 0.012$. The other envelope corresponds to the damping ratio of $\xi = 0.002$ and it fits the response for $t > 1.45\ s$, which is linear. The middle part of the time history can be considered as a transition interval between the nonlinear and the linear response. We can improve the accuracy of this approximation by increasing the number of envelopes, and the limit case corresponds to the method for the calculation of the discrete damping ratios, described in Subsection 2.4.1.

To approximate the nonlinear damping characteristics of the BBSC, a function that fits the discrete damping data is required. This function is found by solving the corresponding optimization problem using the Matlab Optimization Toolbox [93]. The adopted model function consists of two decaying exponential functions, $f_m = b_1 e^{a_1 t} + b_2 e^{a_2 t}$. Coefficients a_i and b_i are found in a least-squares sense by minimizing the square error between the measured input data and the model function. The lower bound for the a_i coefficients is set to zero. In this way, the adopted model function can represent both the nonlinear and constant parts of damping [62]. In order to get the global optimum, the multistart procedure is applied and the optimization problem is solved for 100 different initial starting

points. More details about the theory and the application of this algorithm can be found in [94].

In this way, the functions that fit the discrete damping ratios are found and the results are displayed in Figs. 11a, 11b, and 11c, while the obtained damping ratios for all experimental models are compared in Fig. 11d. The obtained results clearly illustrate the

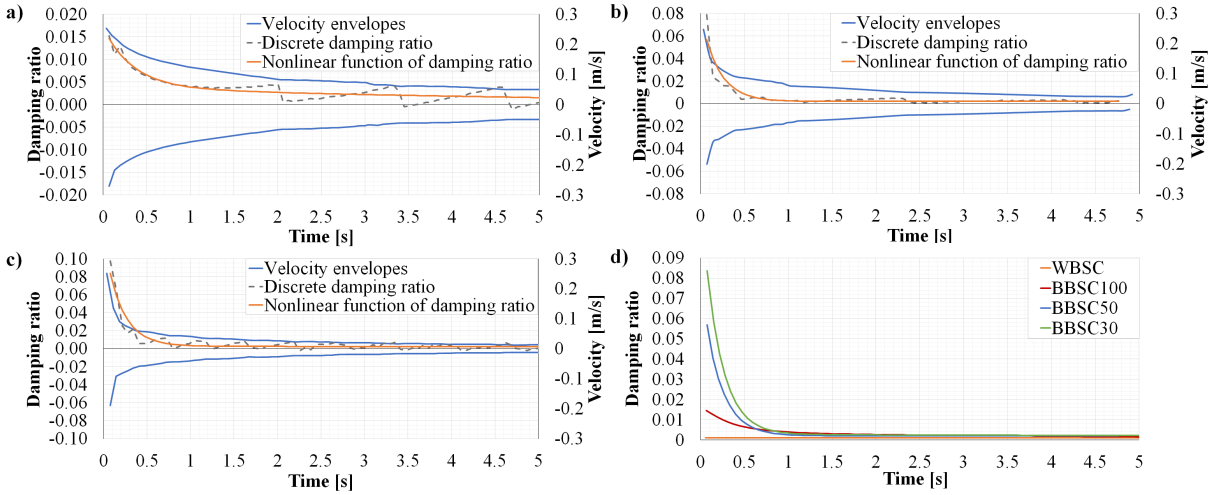

Figure 11: Velocity amplitudes, discrete damping ratios and nonlinear function of damping ratio for: a) BBSC100, b) BBSC50, c) BBSC30. d) Comparison of damping ratios for all experimental models.

strong influence that the bolt tightening forces have on structural damping. Furthermore, the nonlinear change of the damping is clearly pronounced during the initial part of the time history. As time elapses, all models slowly approach the constant value of damping. Thus, after enough energy is dissipated through the structural damping, the slipping in the BBSC deactivates, and the beam continues to oscillate with material damping.

3 Numerical analysis

3.1 Introduction

A well-known commercial FE software Abaqus is used for the numerical analysis. There are several different methods available in Abaqus for performing dynamic simulations. The linear modal analysis is sufficient for the calibration and verification of the numerical WBSC model. For the nonlinear dynamic analysis of the BBSC model, two methods are available: Abaqus/Standard which uses an implicit, and Abaqus/Explicit which uses an explicit time integration algorithm. The explicit approach was utilized here for the reasons discussed below.

An implicit dynamic procedure requires an iteration process to find the equilibrium at an unknown configuration. For complex contact problems with many interacting parts, the implicit method is usually not recommended [8, 88, 89]. The main issue is the change in contact status during a single time increment, which negatively affects the convergence of the nonlinear solver and yields small-time increments. For an analysis with many contact conditions, this issue makes the implicit algorithm computationally expensive.

The considered BBSC model falls into this category due to the contacts between its beam parts, bolts, nuts, washers, and splice plates.

Unlike the implicit, the explicit dynamic analysis efficiently calculates large numbers of small-time increments using the central difference rule. In comparison with the implicit analysis, each increment is relatively inexpensive since the formation and inversion of the tangent stiffness matrix are not required. An important feature is that contact conditions are not of significant concern in an explicit analysis. The contact surfaces can be left in a non-contact state, rigid body movements are acceptable, and the algorithm automatically picks up the stiffness when contact is detected.

The stability limit of a time increment is the main issue of an explicit solver. The time increment is usually adopted as the smallest time required for the stress wave to travel through the smallest element dimension in the model. To satisfy this condition for fine meshes and high-speed wave propagation, the time increment must be very small. When dealing with the BBSC model, it was important to find a balance between the accuracy and the computational time because: (i) the numerical model is relatively large with a lot of contacting surfaces that require fine meshes, (ii) the response time is 6.5 s, which is quite long for an explicit simulation. For this, we had to optimize the FE mesh and find an appropriate stable time increment.

One standard method for limiting the value of the stable time increment is *mass scaling*. When applied properly, the method can significantly improve efficiency by increasing the time increment. In order to minimize the error, mass scaling must be carefully applied to a set of elements that control the increment size. Failure to do so can result in large artificial inertial forces that can significantly affect structural response.

The reliability of explicit nonlinear simulations is commonly assessed via energy outputs. The artificial energy should be small in comparison to internal energy, while the total energy of the overall model should be approximately constant [88].

Our numerical model is relatively complex, and it was adopted through an iterative procedure. The most important parameters that were calibrated via this process are: the FE mesh, boundary conditions, load function, contact formulation, mass scaling, reduced integration, and bulk viscosity. Furthermore, the explicit analysis does not support the bolt force option, and the bolts had to be tightened in line with the temperature change. The calibration and the adoption of these parameters are discussed further in this section.

Regarding the material model, the bilinear stress-strain relationship is adopted. The beam and the splice plates have the following material properties: modulus of elasticity $E = 200\ GPa$, Poisson's ratio $\nu = 0.3$, yield stress $f_y = 235\ MPa$, tensile strength $f_u = 360\ MPa$, and ultimate strain $\epsilon_u = 26\ \%$. For the bolts, nuts, and washers, the same values of E and ν are used, while $f_y = 640\ MPa$, $f_u = 800\ MPa$, and $\epsilon_u = 12\ \%$ [79].

3.2 Numerical model

3.2.1 Finite element mesh

To improve the balance between efficiency and accuracy, the mesh optimization and model reduction are considered. The main steps in these procedures are displayed in Fig. 12. The reference numerical model (NUM1) had all parts of the real structure. The beam is connected to the connecting and carrying plates via rigid angles, while the carrying plate is bolted to the 1×1 m section of the concrete wall that is clamped along its

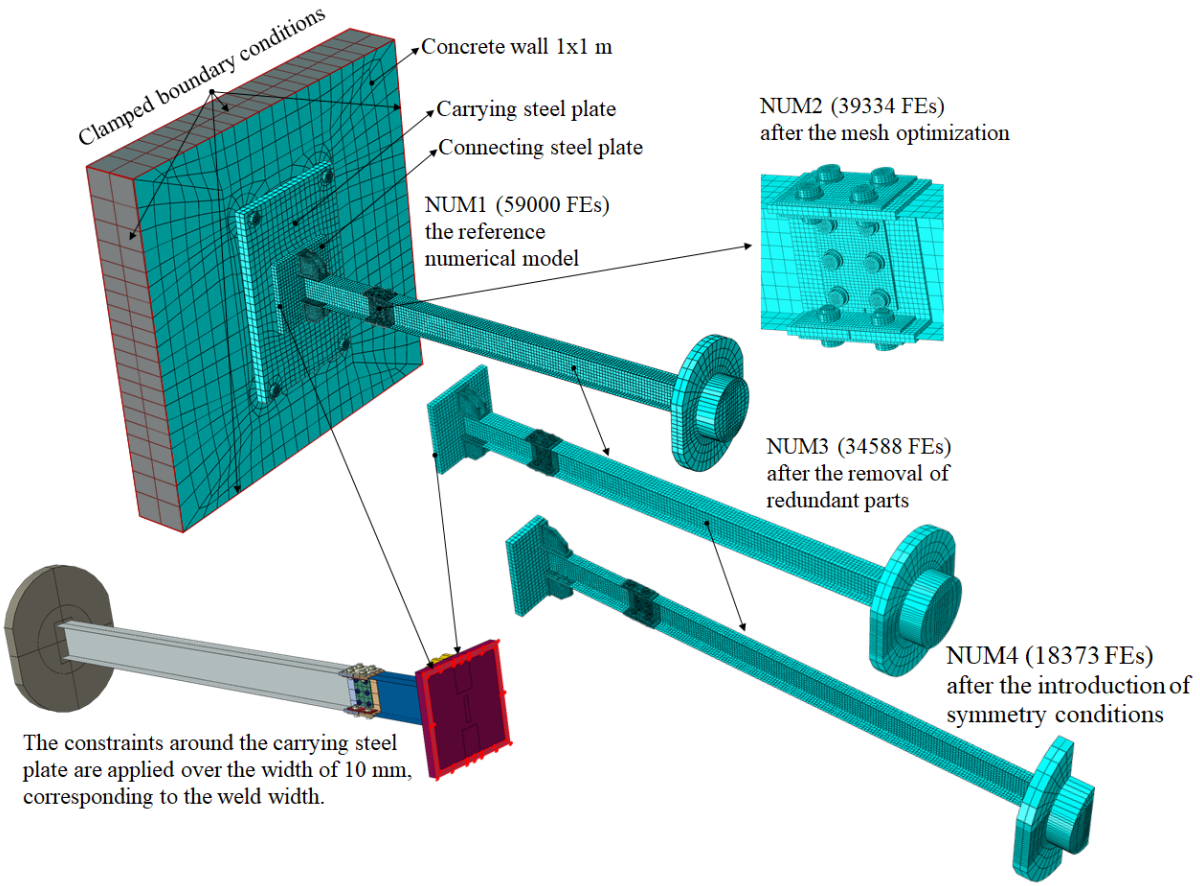

Figure 12: Optimization of the FE mesh and the model reduction.

edges. This model is meshed with 59000 C3D8R brick elements. To optimize the mesh, the beam is meshed with S4R shell elements, except for the connection itself, which is meshed with C3D8R elements. As a result, model NUM2 with 39334 FEs is obtained. Next, our numerical tests suggest that the concrete wall and the carrying plate can be removed. However, this requires fixing of the connection plate along its edges and across 10 mm width, which corresponds to the weld width, see Fig. 2. The obtained model has 34528 FEs and it is designated as NUM3. The FE mesh of this model is given in Fig. 13. Connections between the shell and solid elements are modeled as shell to solid coupling, while the welds are modeled as tie constraints. The thickness of the welds is taken into account, and the WBSC model is also shown in Fig. 13.

Finally, by introducing the symmetry conditions and additional mesh refinement, the NUM4 model with 18373 FEs is obtained, Fig. 12. The initial NUM1 mesh is reduced approximately by a factor of 3. The adopted NUM4 model is verified through a comparison with the NUM1 model. The acceleration time histories, obtained using linear modal analysis, are compared. The agreement between the results is satisfactory, and the NUM4 model is adopted for further consideration. The results are omitted for the sake of brevity.

3.2.2 Contact modeling

The contact modeling is crucial for the analysis of the BBSC model due to contact interactions between different surfaces and associated effects of the local stick/slip behavior. A

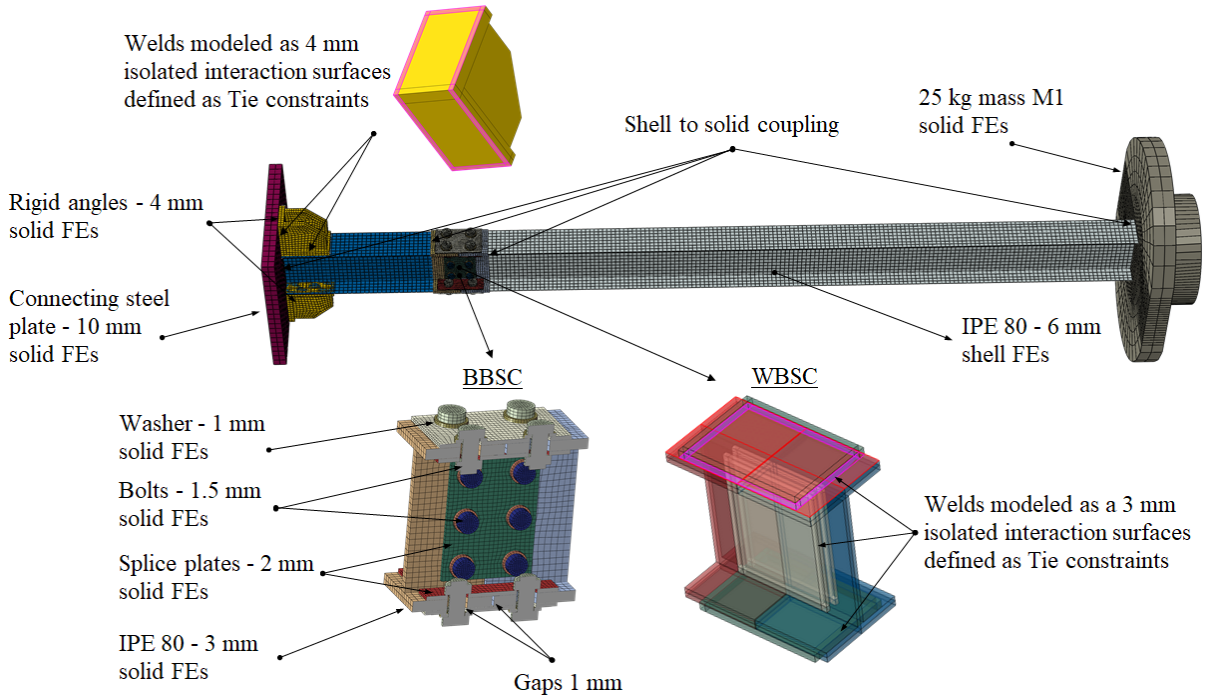

Figure 13: NUM3 model. Types of elements and their approximate dimensions. Application of shell to solid coupling and tie constrains between parts of the model.

considerable effort is required for the calibration of interaction properties and master/slave surfaces. A common algorithm for contact problem solving is the penalty method which is available in both Abaqus/Explicit and Abaqus/Standard. Other approaches, such as the Lagrange multiplier method, or the Perturbed and Augmented Lagrangian methods, are available in Abaqus/Standard only [88, 89].

Abaqus/Explicit offers two contact algorithms: general contact (GC) and contact pair (CP). Both of them have advantages and disadvantages that depend on the problem size, required level of detail, expected accuracy, etc. [24, 25, 89]. The main difference between these two contact algorithms is contact discretization. The GC method uses node-to-surface, while the CP algorithm employs surface-to-surface discretization. GC is a robust, accurate, and efficient algorithm that allows straightforward modeling of contact interactions between multiple bodies. The node-to-surface discretization is a point-to-surface method where each contact constraint involves a slave node and a master face. One issue of this approach is the penetration of slave surfaces by master nodes, which affects the solution. A mesh refinement of slave surfaces is a simple way to tackle this issue.

On the other hand, the CP algorithm is not as simple to use as GC. It requires an explicit definition of all interacting surface pairs, along with the properties, constraints, and master/slave surfaces for each contact pair. The surface-to-surface formulation detects contact conditions in regions around the slave nodes, rather than only at the individual slave nodes. These regions are approximately centered around slave nodes, so each contact constraint predominantly utilizes one node, but also considers the adjacent ones. The surface-to-surface algorithms do not suffer from the penetration issues between nodes and master/slave contacting surfaces. Unlike the node-to-surface, the surface-to-surface algorithms are not sensitive to the master/slave roles between contacting surfaces. Fur-

thermore, they can reduce local penetrations and improve the accuracy of contact stresses even for non-matching meshes. However, it is recommended that the slave surface has denser mesh than the master surface, while the stiffer body should be assigned as a master.

Both the GC and CP algorithms were utilized here for the analysis of the BBSC model in order to investigate their pros and cons. Contact interaction was defined between all components of the BBSC: the beam parts, bolts, washers, and splice plates. To simplify the GC numerical model, the individual surface pairs that are expected to interact are defined. Since GC supports the definition of multiple interacting surfaces between different parts, the BBSC was modeled with 24 individual contact pairs. Regarding the CP approach, each contact interaction pair needs to be defined. Also, contact interaction can consist of only one surface from each of the two parts. These requirements resulted in 69 contact surface pairs for the CP model. The balanced master/slave weighting is applied for both GC and CP, and the weighting factor is set to $f = 0.5$ for the CP case.

Let us emphasize that we used GC for the major part of our research, due to its simplicity. Therefore, all the presented results, until Subsection 3.4.4, are given for the GC contact algorithm.

Contact interaction along the normal direction is defined as normal hard contact, allowing the separation between the interacting surfaces. The isotropic Coulomb's law of friction assumes that there is no relative tangential motion when the frictional shear stress is less than some critical stress that is proportional to contact pressure. Even for models without relative sliding, the numerical implementation of the Coulomb friction through the penalty method allows some elastic slipping in contact interaction due to the finite stiffness of penalty springs. As mentioned in Section 1, the coefficient of friction has a crucial role in the analysis of mechanical connections and it can strongly affect nonlinear structural response. For the friction between steel surfaces, the friction coefficient varies from 0.1 to 0.8 [15–17, 24, 39–41, 79]. This broad range of values is caused by a variety of parameters that influence friction, as discussed in Section 1. We conducted detailed numerical analyses to find the most suitable friction coefficient for the problem at hand, and the value of $\mu = 0.155$ was adopted. A similar value for the friction between steel parts can be found in works that investigate bolted connections [15, 39, 95–97]. The penalty friction method with finite sliding, based on Coulomb's law of friction, is utilized for the tangential contact behavior.

3.2.3 Tightening of bolts

A standard bolt connection consists of a bolt, nut, and washer. To limit the number of contact surfaces, the bolt and nut are here modeled as a single body, Fig. 14a. Abaqus supports two methods for the modeling of bolt tightening by: applying a bolt force and adjusting the length of the bolt shank. However, these options are not supported in Abaqus/Explicit.

Several approaches for the tightening of bolts in Abaqus/Explicit can be found in the literature. One is called turn-of-nut [98] and it is based on detailed modeling of threads on the shank and inside the nut. The bolt pretension is then introduced by rotating the nut. Another approach is to apply a temperature change to either the bolt shank [8] or to the washer [99, 100]. The latter approach was employed in our numerical model by applying a temperature change to the washer.

The washer was made from an orthotropic material with a non-zero thermal expansion coefficient only along the bolt direction, Fig. 14a. Prior to the application of mass M2,

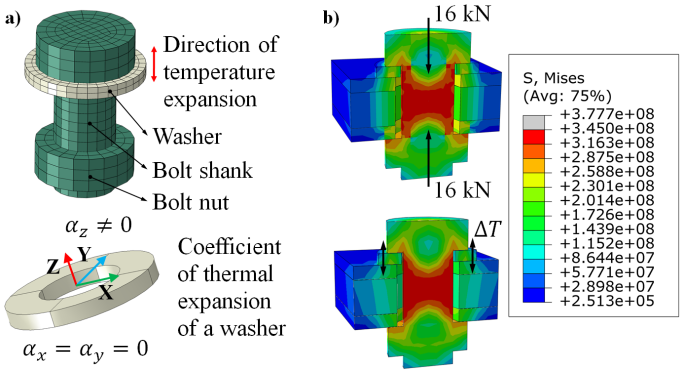

Figure 14: Tightening of bolts. a) Model of a bolt, nut, and washer. The thermal expansion coefficients for the washer. b) Distribution of the von Mises stresses for the bolt force and temperature change methods.

the washer was subjected to the positive a temperature change, causing volume expansion along the z direction and producing tension in the bolt shank. With proper calibration of the temperature load, the required tightening force was obtained. For verification purposes, a numerical model with static bolt force was made in Abaqus/Standard. The von Mises stress distributions in the bolt at the final step of loading are displayed in Fig. 14b. The stresses are the same for both the temperature method and the bolt force procedure.

3.3 Validation of the numerical model

The calibration, verification, and validation of numerical models are complex processes. They require many iterations in which various properties of the experimental and numerical models must be compared. Details on the calibration and verification are given in Subsection 3.4. Here, we are presenting the results obtained with the adopted numerical model and compare them with the experimental data. The first step of the validation is the modal analysis, while the velocity time histories are compared afterward.

3.3.1 Modal analysis

The experimental ASR results for the BBSC and WBSC models are given in Subsections 2.2.1 and 2.2.2. The numerical BBSC model, adopted in Subsection 3.2.1, has eigenfrequencies of 15.61 Hz, 15.58 Hz, and 15.55 Hz for 100 %, 50 %, and 30 % of the bolt tightening force, respectively. These values are in good correspondence with the experimental results given in Fig. 6, and are a bit higher than that of the initial numerical model, Fig. 3. Actually, the differences with respect to the experimental results are less than 2.5%. It should be emphasized that the modal analysis was done in Abaqus/Standard after a static step for the tightening of bolts. However, the influence of the bolt tightening force is small because the main nonlinear effects due to the deformation and slipping inside the connection were not captured with our numerical modal analysis.

Regarding the considered eigenfrequencies of the WBSC model, their experimental values are given in Fig. 8. Numerically obtained values are 15.7 Hz and 20.5 Hz, and they differ from the experimental ones for approximately 3% and 6%, which is an acceptable alignment of results for the free vibration test.

3.3.2 Velocity time histories

The velocity time histories obtained with the adopted numerical BBSC models are compared with the experimental results in Figs. 15, 16, and 17. The experimental and nu-

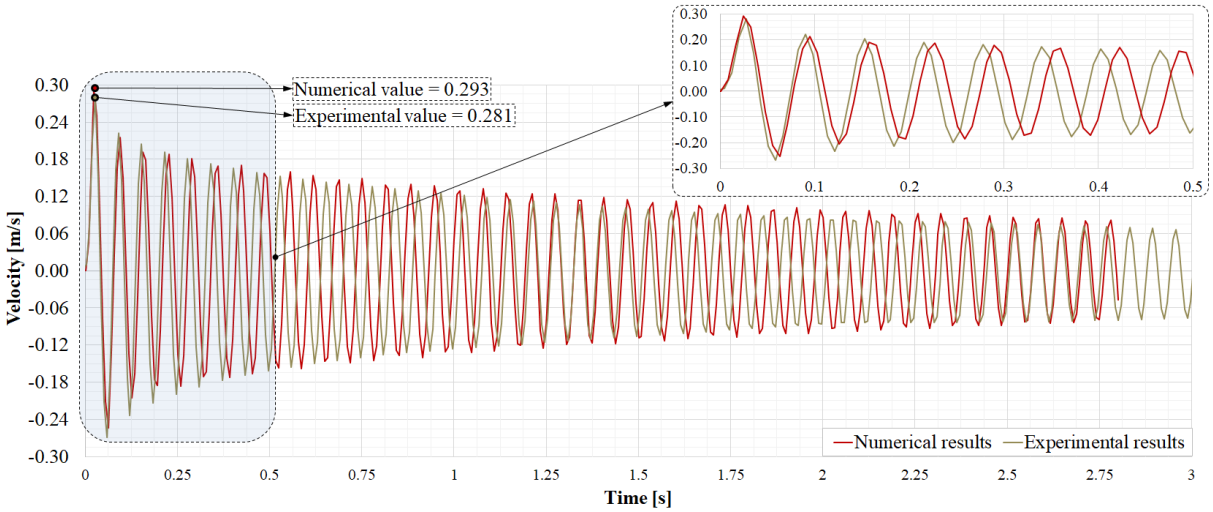

Figure 15: Bolted beam splice connection with 100 % of the bolt tightening force - BBSC100. Comparison of experimental and numerical velocity time histories.

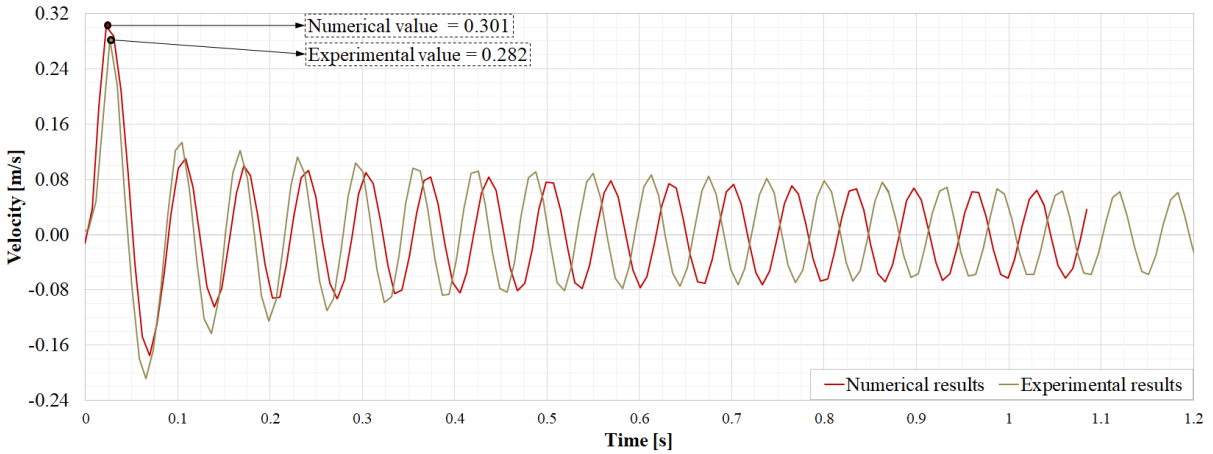

Figure 16: Bolted beam splice connection with 50 % of the bolt tightening force - BBSC50. Comparison of experimental and numerical velocity time histories.

merical responses agree reasonably well, considering the complexity of the problem. The excellent correspondence of the first amplitudes is emphasized in the graphs. The agreement of the results deteriorates with the decrease of the bolt tightening force. Furthermore, it is evident that all experimental models oscillate with somewhat higher frequencies in comparison with the numerical models, which causes a small time shift between the compared responses. The differences between the eigenfrequencies are already discussed in the previous subsection. These differences are more pronounced in the velocity time histories due to the significant nonlinearity of the considered responses.

All in all, the agreement between the experimental and numerical results validates our adopted numerical model. This is particularly true for the BBSC100 model which is the

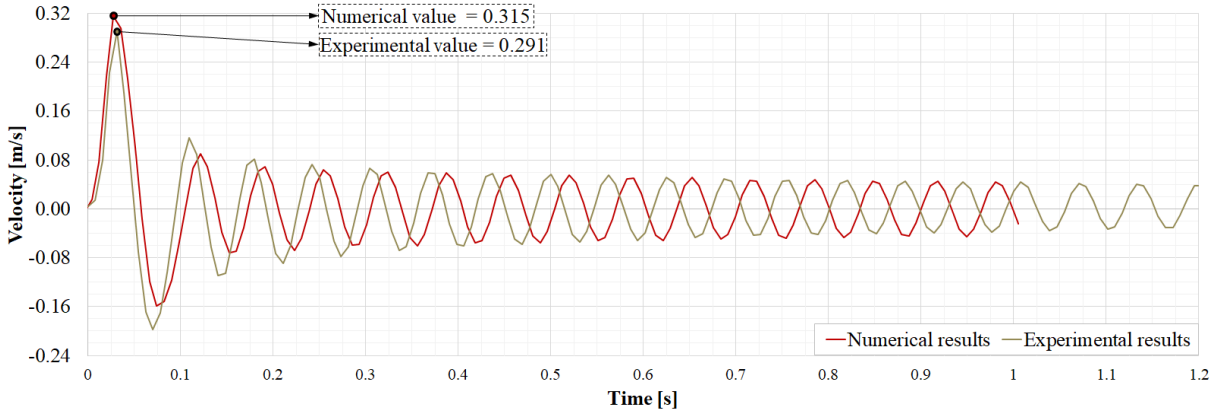

Figure 17: Bolted beam splice connection with 30 % of the bolt tightening force - BBSC30. Comparison of experimental and numerical velocity time histories.

focus of our research.

3.4 Calibration and verification of the numerical model

In this subsection, the calibration and verification of the main parameters are considered. First, we are calibrating the load function that is separated into two parts: load application and load release functions. This is followed by a discussion and verification of proper mass scaling. Then, the influences of bulk viscosity, order of numerical integration, and contact formulation on structural response are considered. Finally, the quality of the numerical solution is assessed through the analysis of the model's energies.

3.4.1 Load release function

Let us consider the load release function that describes the removal of additional mass M2. Since the load release time Δt_{LR} is relatively short, the linear function was adopted. The experimental results in Fig. 5 suggest that the bolt tightening force does not significantly affect the first amplitude of acceleration. Due to this fact, the load release time was calibrated with respect to the first acceleration amplitude. Five different load release time intervals are tested via the modal dynamic analysis using $\xi = 0.012$, see Fig. 10. The envelopes of numerically obtained accelerations and the experimental acceleration time history are shown in Fig. 18a. The obtained envelopes reveal that the first amplitude converges with respect to the load release time. Therefore, the value $\Delta t_{LR} = 0.015\ s$ was adopted in our numerical model.

The first 0.4 seconds of the acceleration and velocity time histories obtained with the modal dynamic analysis and compared with the experimental results are displayed in Figs. 18b and 18c. Using the adopted load release time, $\Delta t_{LR} = 0.015\ s$, the numerical and experimental results agree reasonably well. Additionally, the adopted load release time is validated by comparing the first velocity amplitudes in Subsection 3.3.2. The experimental and Abaqus/Explicit results are in good agreement, see Figs. 15, 16, and 17. The relative difference between the first velocity amplitudes for the BBSC100 model is around 4 %, and increases as the bolt tightening force decreases.

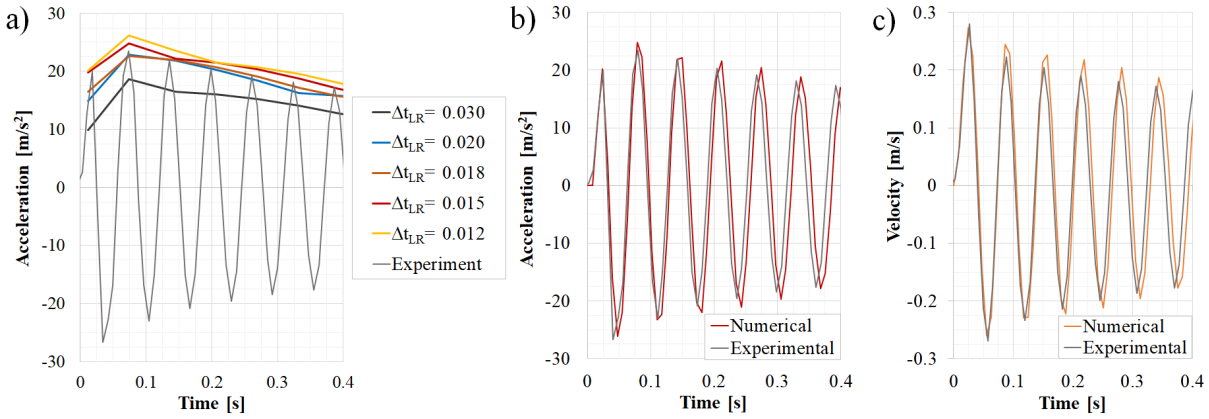

Figure 18: Calibration of the load release time with respect to the first experimental amplitude. a) Envelopes of acceleration for different values of the load release time Δt_{LR}. b) Acceleration time history with $\Delta t_{LR} = 0.015$. c) Velocity time history with $\Delta t_{LR} = 0.015$.

3.4.2 Load application function

In order to find the balance between efficiency and accuracy, it was necessary to adopt an appropriate load application function. After several tests, the circular function and the load application time $\Delta t_{LA} = 3.5\ s$ were adopted, see Fig. 19. The load function is defined in the time interval $t \in [-3.515, 0]$, while the pretension of bolts takes place for $t \in [-3.715, -3.515]$. After the load release, the free vibration response occurs during the interval $t \in [0, 2.8]$. The displacement time history in Fig. 19 clearly indicates a significant sudden movement after approximately 0.5 s of load application. This large displacement is caused by the macro slip in the bolted connection, which was also observed in the experiment, see the numerical and experimental BBSC in Fig. 19. Due to this slip, the right part of the beam suddenly rotated with respect to the clamped part, causing the splice plates to bend. The result is a complex stress state in the connection, which will be presented in Subsection Fig. 3.4.4. After the initial macro slip and the load release, the beam oscillated with respect to a newly found static equilibrium position.

In order to scrutinize the influence of load application time, the velocity time histories for three values of Δt_{LA} are shown in Fig. 20. Regardless of the load application time, the macro slip occurred. The main difference between obtained responses is that, for $\Delta t_{LA} = 5.5\ s$, the velocity amplitudes almost completely dampen before the load release, in contrast to the other two models. The full damping of the structure before the load release would be an ideal case, but also non-efficient due to the large load application time. Actually, the point of this calibration was to test the influence of the vibrations remaining after the load application on the free vibration response. The obtained results suggest that the velocity responses of models with $\Delta t_{LA} = 3.5\ s$ and $\Delta t_{LA} = 5.5\ s$, for $t > 0$, are practically indistinguishable, while the model with $\Delta t_{LA} = 2.5\ s$ gives similar amplitudes but is slightly shifted in time. These observations provided an argument for adopting the value $\Delta t_{LA} = 3.5\ s$.

Regarding the displacement time histories, it is evident that the model with the slowest application of load, $\Delta t_{LA} = 5.5\ s$, had the smallest displacement. Also, the slipping of this model occurred in two instances, and its value was lower than that of the other two models. If we focus on the instances when the slipping occurred, it is evident that

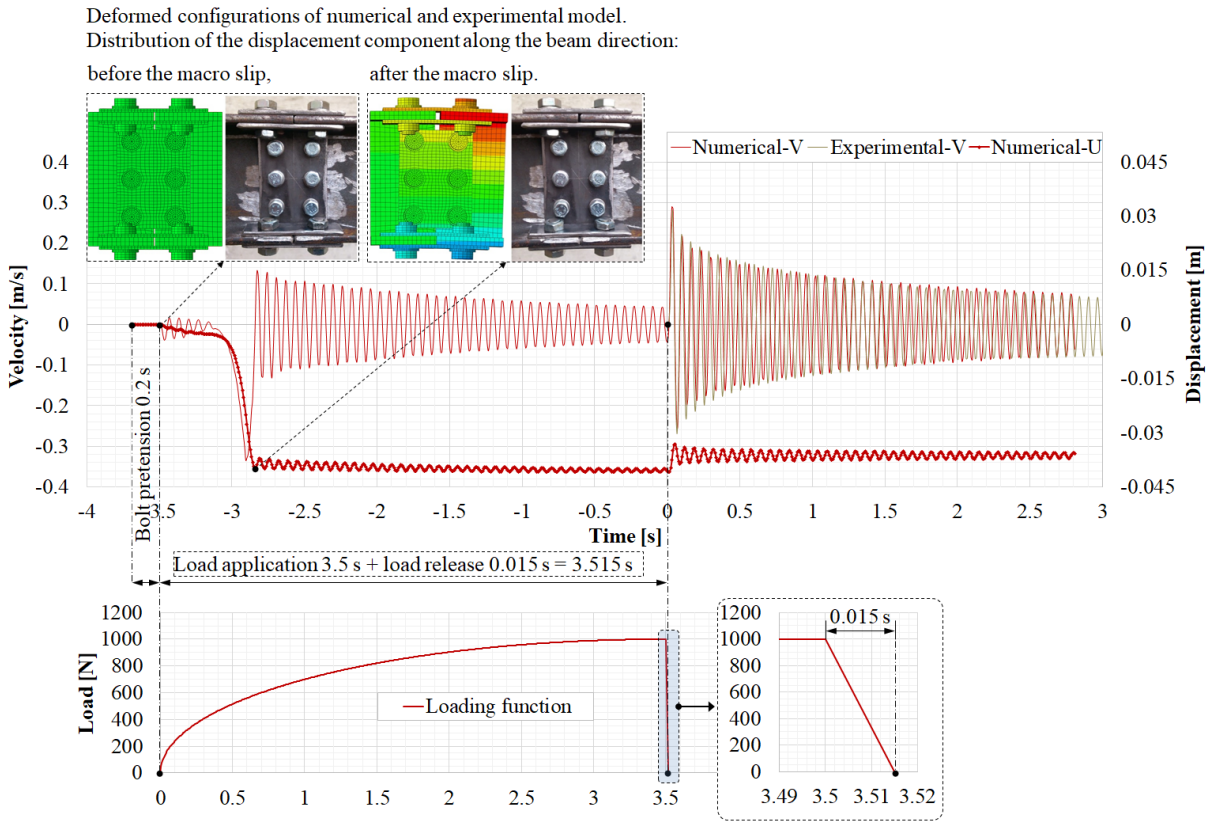

Figure 19: Adopted load function. The velocity and displacement time histories for the adopted load function. The physical and numerical model of the BBSC before and after the macro slip.

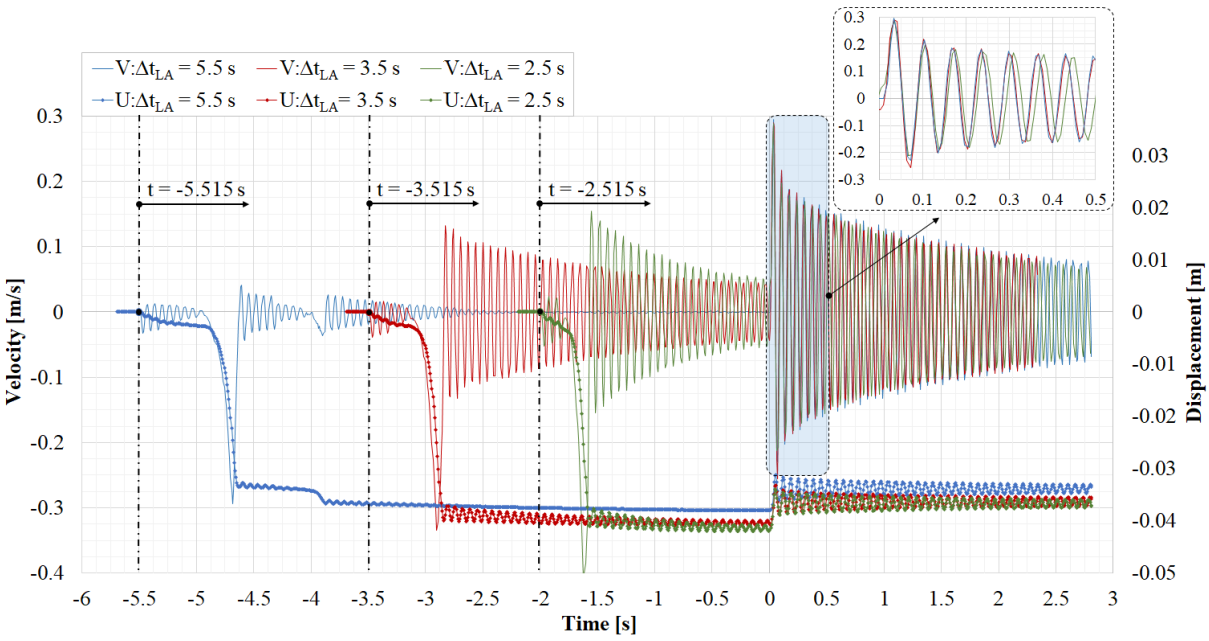

Figure 20: Calibration of the load application time for BBSC100. Velocity and displacement time histories for: $\Delta t_{LA} = 2.5\ s$, $\Delta t_{LA} = 3.5\ s$, $\Delta t_{LA} = 5.5\ s$.

the velocity peak increases with the decrease in the Δt_{LA}. This can cause significant disturbance of the free vibration response, especially if the load application time reduces below 1.5 s.

3.4.3 Mass scaling

As already discussed, the crucial parameter of explicit time integration is the stable time increment. Its correct value is vital for the accuracy of numerical results, and it strongly affects computational time. Since the adopted numerical model initially required approximately 110 h of computation for 6.5 s of simulation, we employed mass scaling to reduce computational time. Mass scaling is a standard procedure for the increase of the stable time increment. This increment is equal to the time required for a wave to propagate through the smallest element dimension, and we can increase it by deliberately increasing the mass density of critical FEs. The application of mass scaling requires special attention in dynamic analysis because it introduces fictitious inertial forces. The task is to carefully select FEs for mass scaling by balancing the computational time and accuracy.

For the adopted numerical model, the selected FEs are shown in Fig. 21. These are the

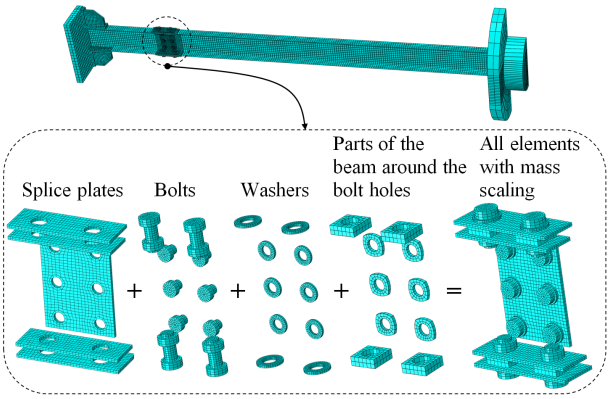

Figure 21: Selected set of finite elements for the application of mass scaling.

smallest FEs in the model and they belong to the splice plates, bolts, washers, and parts of the beam around the bolt holes. The crucial step was to investigate the influence that mass scaling had on structural response. For this, three values of the stable time increment were tested: $\Delta t = 9.83 \times 10^{-8}$ s, $\Delta t = 2.00 \times 10^{-7}$ s, and $\Delta t = 3.40 \times 10^{-7}$ s. The reference model was the one without mass scaling, with the time increment $\Delta t = 9.83 \times 10^{-8}$ s.

The velocity time histories for these three values of Δt are shown in Fig. 22. Evidently, the model with the stable time increment of $\Delta t = 2.00 \times 10^{-7}$ s returned the same results as the reference model without mass scaling. On the contrary, the model with $\Delta t = 3.40 \times 10^{-7}$ s gave significantly different results. Following these observations, the mass scaling that returned the stable time increment of 2.00×10^{-7} was adopted in our numerical model. As the result, the initial stable time increment was increased by a factor of 2.03 without significantly influencing the structural response.

Additionally, the mass increase for the whole model and selected elements is depicted in Fig. 22. The mass increase of the adopted model is 1.73% for the complete structure and 145% for the selected elements. Although the mass increase of selected elements was substantial, the mass increase of the whole model was negligible and the influence of fictitious inertial forces was insignificant. For the model with $\Delta t = 3.40 \times 10^{-7}$ s, the

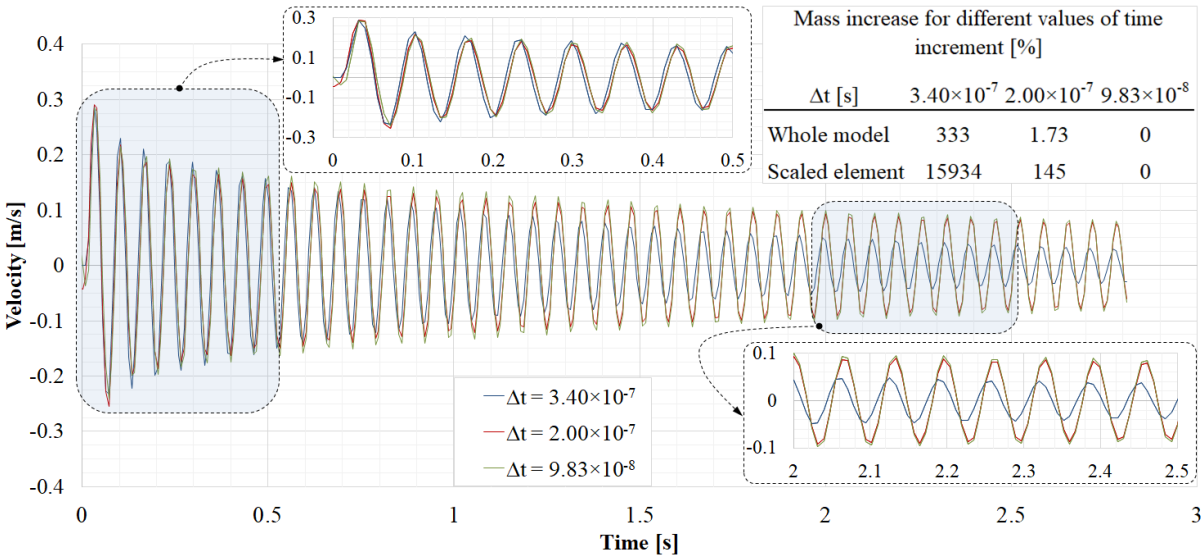

Figure 22: Verification of mass scaling on BBSC100. Velocity time histories and mass increases for three models with different values of stable time increment Δt.

whole mass increased by a factor of 3.3, while the mass of selected elements rose by a factor of 160. This large increase of mass caused evident errors in the numerical response.

The reference numerical model, without mass scaling, required 110 h of computational time for 6.5 s of simulation. By applying the adopted mass scaling, the computational time was reduced to approximately 53 h, which greatly improved efficiency. Let us note in passing that computational time depends on several other parameters besides mass scaling, the order of numerical integration being the most important. In comparison with the reduced spatial integration, the full integration increased computational time of our model, on average, by more than 200%.

3.4.4 Bulk viscosity and order of integration

There are two sources of energy dissipation in our BBSC numerical model: nonlinear damping due to the friction in the bolted connection and numerical damping. Let us focus on numerical damping. Two main sources of numerical damping in Abaqus/Explicit are bulk viscosity and the order of integration. Bulk viscosity represents artificial damping proportional to volumetric straining. The addition of such a viscous pressure term to the equation of motion helps to solve high-speed dynamic events. The method is also known as the von Neuman-Richtmeyer viscosity [101, 102]. Bulk viscosity in Abaqus/Explicit consists of linear and quadratic terms, and the default values were used for our numerical model.

In order to model contact in the bolted connection, linear fully-integrated C3D8 elements were initially used for the splice plates, parts of the beam, washers, etc. Such a modeling approach causes issues with bending deformations. Concretely, a strong shear locking effect occurs and artificially increases the stiffness of the structure. This issue is alleviated by the implementation of the C3D8R elements with reduced integration. However, an unwanted side effect of the reduced integration is hourglassing, the distortion of elements that occurs during the bending if the mesh across the thickness dimension is sparse [88, 103, 104].

Bearing this in mind, we analyzed the numerical damping that exists in our explicit simulations. In order to exclude structural damping, the WBSC model was considered. The adopted numerical model utilizes both the bulk viscosity and C3D8R elements. The obtained results are omitted for the sake of brevity, and the resulting numerical damping is close to 0.001. This value is in excellent agreement with the material damping discussed in Subsection 2.2.2. Therefore, the numerical damping of the adopted numerical model corresponds to the estimated material damping of the real structure. Due to this fact, there is no need to explicitly define damping in our numerical model. Moreover, these values of the material and numerical damping are not crucial for the observed response, which is dominated by structural damping due to friction, see Fig. 11. The main source of numerical damping in our case is reduced integration, and its effect can be alleviated by increasing mesh density along the thickness direction.

Let us consider the influence that bulk viscosity and the order of integration have on the BBSC100 model response. Both the GC and CP contact formulations are considered, and the velocity time histories are given in Figs. 23 and 24. Furthermore, the distributions

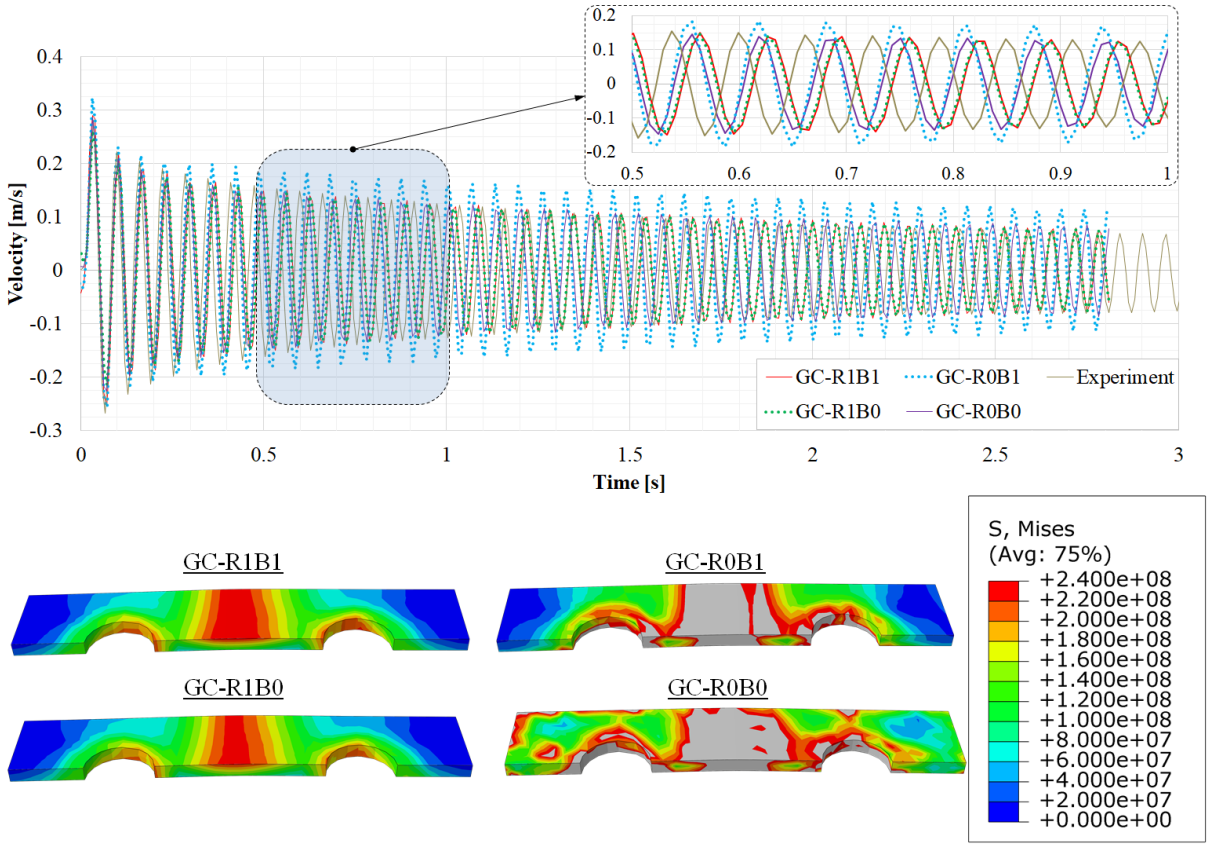

Figure 23: Influence of bulk viscosity (B) and the order of integration (R) using the General contact (GC) formulation. Velocity time histories. Stress distributions in the flange splice plate at the upper part of the section, before the load release.

of Mises stress in the flange splice plate at the upper part of the section, before the load release, are shown. Different models are marked as RxBx, where x takes the value of 0 or 1, while R and B represent abbreviations for **R**educed integration and **B**ulk viscosity, respectively. x=1 indicates that a parameter is included, while x=0 designates that a parameter is excluded.

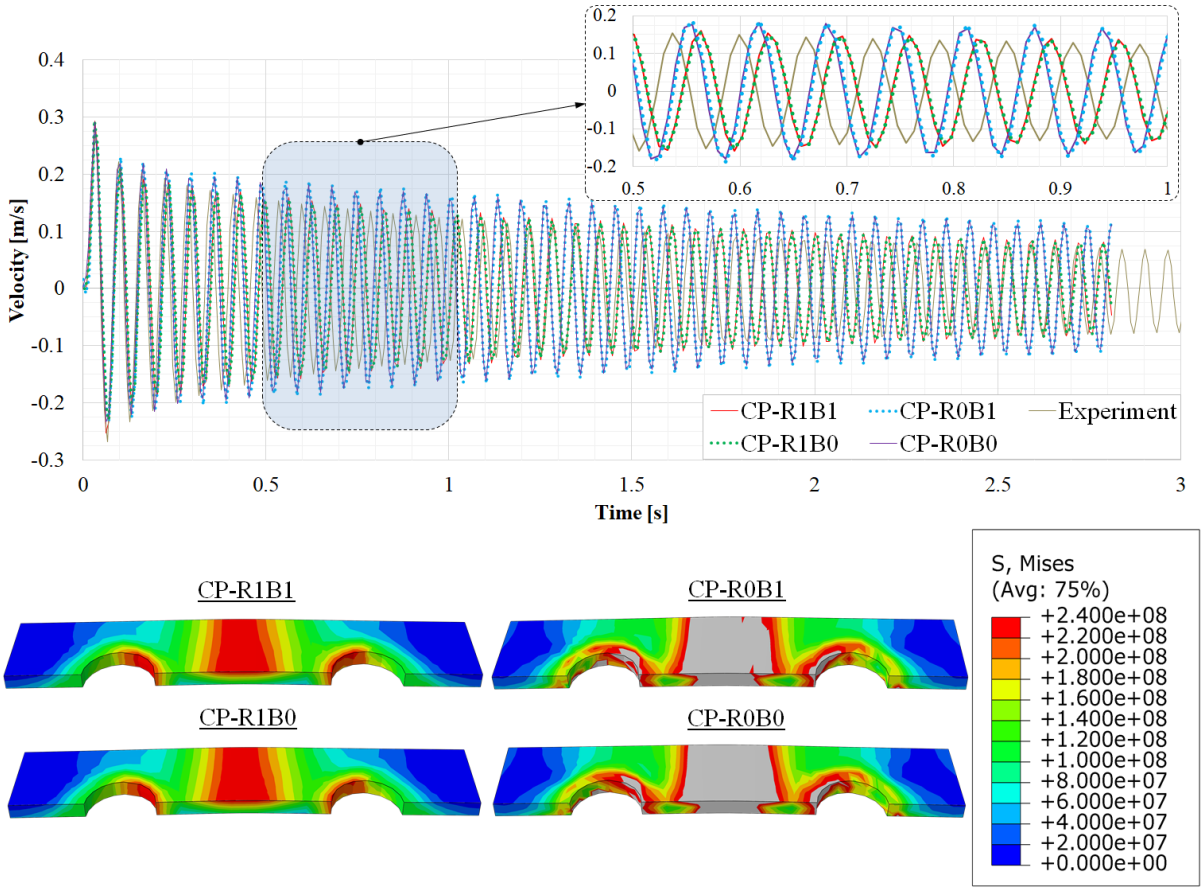

Figure 24: Influence of bulk viscosity (B) and the order of integration (R) using the Contact pair (CP) formulation. Velocity time histories. Stress distributions in the flange splice plate at the upper part of the section, before the load release.

All the results that were presented until now were obtained with the GC R1B1 model. The most important observation from the results in Figs. 23 and 24 is that the R1B1 models are invariant with respect to the contact formulation. For the C3D8R elements, bulk viscosity does not influence velocities, but it does affect stress distributions, which is more pronounced for the GC formulation.

Regarding the fully integrated C3D8 elements, they return erroneous results. The dominant eigenfrequency of the C3D8 models is invariant with respect to the contact formulation and bulk viscosity, and its value is a bit higher than that of the C3D8R models. This happens due to shear locking. Regarding the velocity amplitudes, they are higher for the C3D8 elements, with the exception of the GC-R0B0 model. The full integration strongly affects stresses and the splice plate plastifies. Finally, the stress distributions obtained with the CP formulation are much smoother than those from the GC approach. In general, the results from the CP formulation are more reliable and independent from other parameters. This is mostly due to the issues inherent in the GC point-to-surface modeling, such as penetration and snugging of master nodes.

3.4.5 Energy considerations

The energies of a numerical model are important parameters that can quantify the quality of the numerical solution. To verify the quality of the solution, four energies are observed: total energy E_{TOT}, internal energy E_I, artificial strain energy E_A, and work done by penalties E_{PW}. Some general guidelines are that E_{TOT} should be constant, while the ratio of E_A and E_I should be less than approximately $2-10\%$, depending on the model [88, 105, 106].

Both contact formulations are considered, and the energy time histories are shown in Figs. 25 and 26. Let us first discuss the total energy. For both contact formulations,

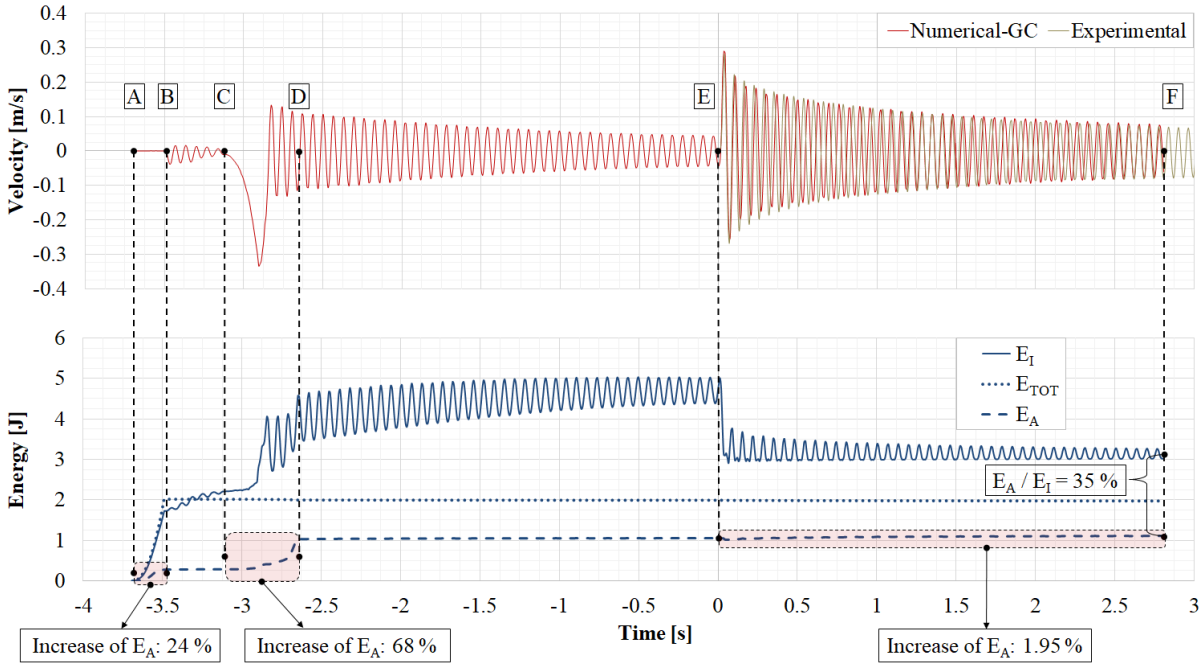

Figure 25: Energy time histories of the GC model. Experimental and numerical velocity time histories.

E_{TOT} increases for a similar value during the bolt tightening in the time interval AB. This occurs because the internal energy increases as a result of the temperature expansion of the washer, but there is no external work. Afterward, the total energy is constant for the GC formulation in the interval BF. However, for the CP formulation, the situation is different. Due to the significant work done by penalties, E_{PW} significantly increases in the interval CD, where the macro slipping occurs. The penalty energy is practically constant in the remaining interval DF, with the exception of small increase at the point of the load release. This increase in E_{PW} is followed by a decrease in E_{TOT}. If we consider E_{TOT} without E_{PW}, the obtained energy is practically constant. This inconsistency is specific to the adopted model with the CP formulation. The problem of non-constant total energy is often present in contact and impact problems [107, 108]. If there is a significant change in E_{TOT}, it is important to double-check the results. In our case, the free vibration velocity time history in the time interval EF is not affected by this phenomenon.

Regarding the ratio between the artificial and internal energy, E_A/E_I, it is 8.5% for the CP, and 35% for the GC formulation. Evidently, this ratio is inside the acceptable limits for the CP, and outside of the limits for the GC formulation. This observation proves that

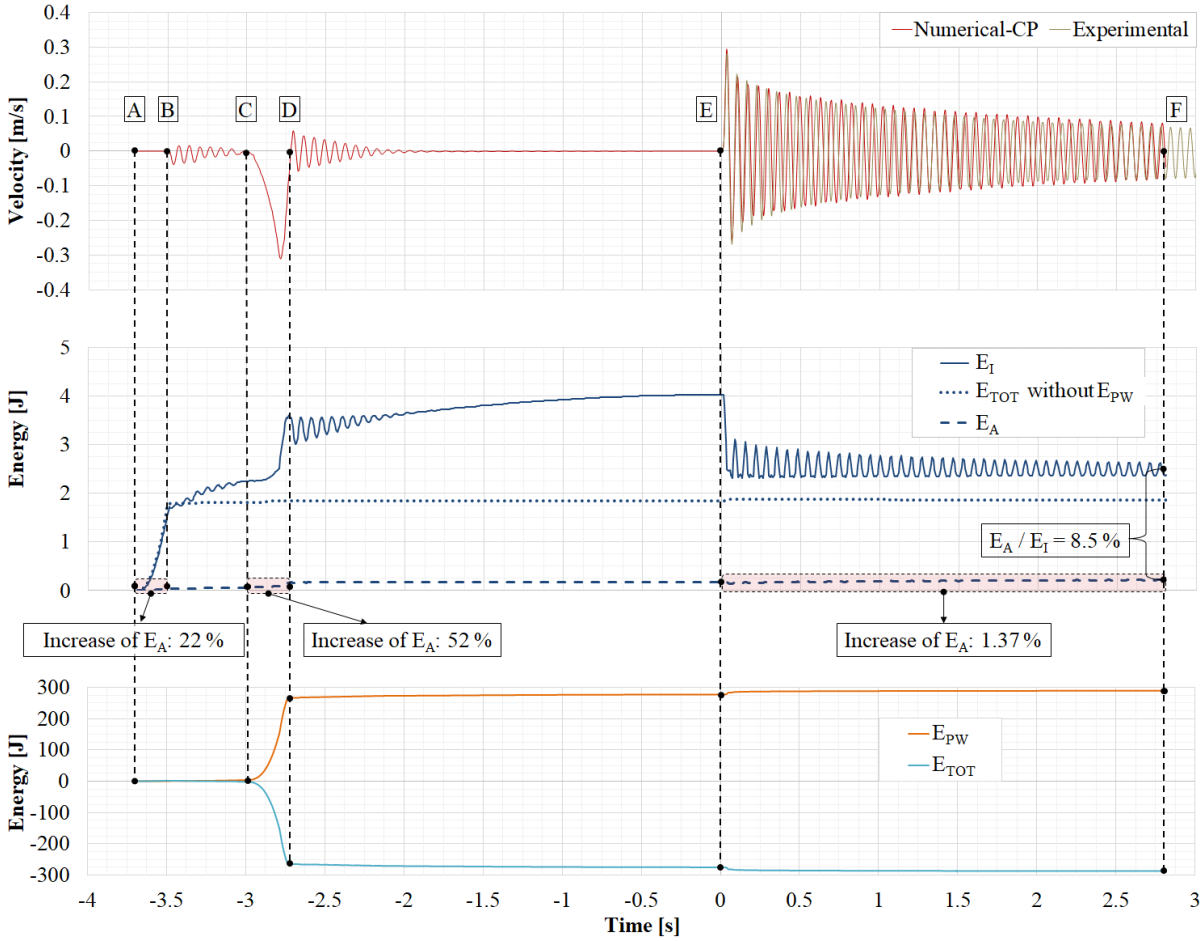

Figure 26: Energy time histories of the CP model. Experimental and numerical velocity time histories.

surface-to-surface contact discretization helps reduce the hourglassing effect. The increase of the artificial energy dominantly occurs during the bolt tightening (time interval AB) and the macro-slipping (time interval CD). The relative increases of E_A that occur during these two intervals are similar for both contact formulations, but the absolute value is higher for the GC formulation by a factor of 5. Since the internal energies are similar in both contact formulations, this directly affects the observed ratios E_A/E_I. The most significant fact is that the relative increase in the artificial energy is negligible during the free vibration response (interval EF).

To scrutinize these observations, the velocity and displacement time histories for the adopted numerical model and both contact formulations are juxtaposed in Fig. 27. First, the free vibration response is not affected by the discussed energy inconsistencies in both contact formulations. The CP formulation fully dampens the vibrations due to the load application, while the remaining vibrations for GC do not affect the free vibration response, as discussed in Subsection 3.4.2. Importantly, the CP formulation returns better contact stress distributions, as shown in Subsection 3.4.4. Therefore, CP is the preferable method for our numerical model, and it is discussed in the following section.

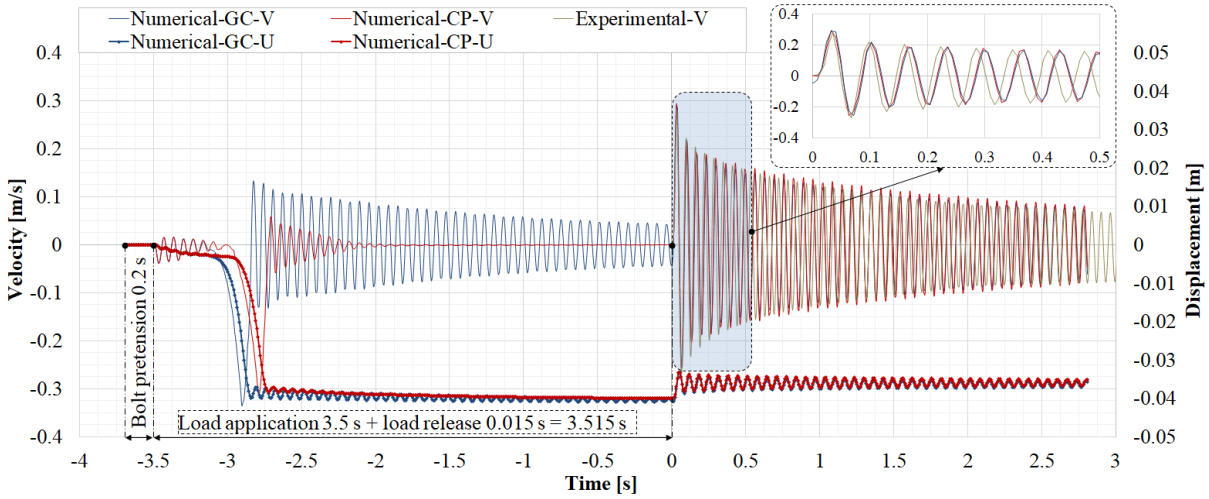

Figure 27: Comparison of experimental and numerical time histories for both contact formulations.

4 Discussion and conclusions

In this section, the main results are discussed and the nonlinear energy dissipation mechanism of the numerical model is scrutinized. The main conclusions are summarized at the end.

In order to properly describe experimental tests, the numerical model had to be deliberately calibrated and verified, see Subsection 3.4. One of the crucial parameters that required calibration was mass scaling. It is often desirable to scale the mass of a system in explicit procedures to allow reasonable calculation times, but this can lead to large errors. Through a careful verification presented in Subsection 3.4.3, it is shown that the adopted mass scaling does not produce significant fictitious inertial forces. Another important parameter of the numerical model is the order of numerical integration. The reduced integration of the C3D8R elements introduces the numerical damping that is practically equal to the material damping of our model. Regarding the contact formulations, both of them return the same velocity time histories, but different stress distributions.

The adopted numerical model is validated through the comparison of the experimental and numerical velocity time histories in Subsection 3.3.2. The experimental and numerical results for the BBSC100 model are in agreement. Also, the correspondence of the results for the BBSC50 and BBSC30 models is satisfactory, considering the complexity of the models and responses. In the following segment, we will be focusing on the BBSC100 model, since it is the one that is readily found in engineering structures.

The most important result of this research is the successful numerical modeling of structural damping due to friction in the BBSC model. Friction is a complicated phenomenon that depends on various parameters, as discussed in Section 1. In the adopted numerical model, friction is introduced via the classic Coulomb's law. This simplified approach is not an accurate representation of friction but returns an acceptable approximation. In order to scrutinize the influence of friction on the response of the BBSC100 model, five simulations with different values of the friction coefficient were considered, and the velocity envelopes are shown in Fig. 28. The model with $\mu = 0.155$ agrees with the experiment, as has been already discussed. Moreover, the results are acceptable for $\mu = 0.2$,

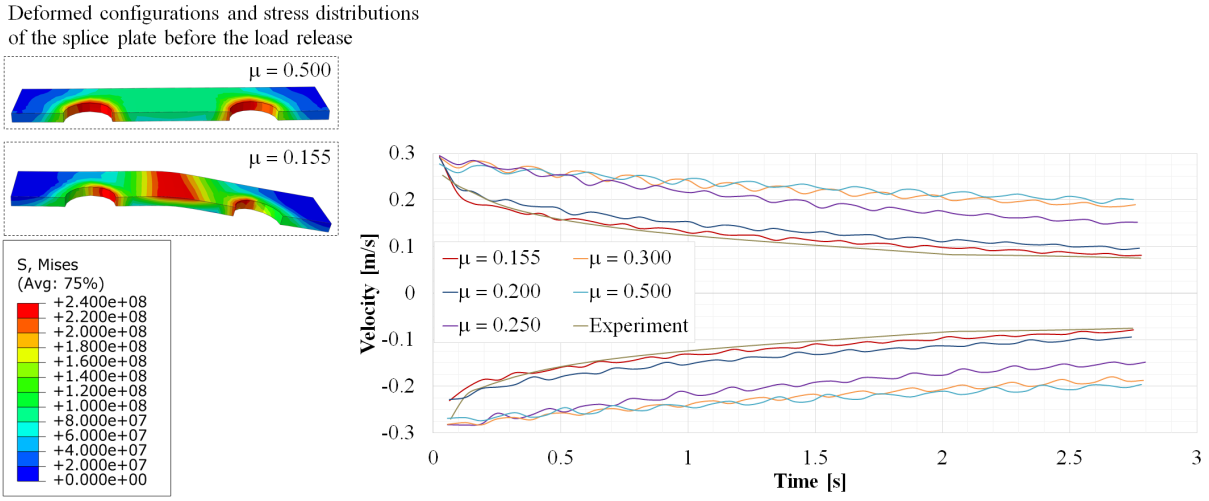

Figure 28: Bolted beam splice connection and 100 % of tightening force. Velocity time histories for different values of the friction coefficient. Deformed configurations and stress distributions in the upper flange are shown for $\mu = 0.155$ and $\mu = 0.500$, at the instance before the load release.

which is actually the value that Eurocode recommends for non-treated steel surfaces [79]. A possible reason for the smaller value of friction in our model is air humidity, see Section 1 and Subsection 2.1.1. Next, the structural response for $\mu = 0.25$ significantly differs, and the nonlinear damping effect almost vanishes. For the friction coefficients $\mu = 0.3$ and $\mu = 0.5$, the results are similar and the response is practically linear. This suggests that, for these friction values, the BBSC does not have a micro slip and it corresponds to the BWSC. This is also evident from the stress distributions in the upper flange splice plate for $\mu = 0.155$ and $\mu = 0.500$, Fig. 28. In contrast to the adopted numerical model with $\mu = 0.155$, the initial macro slip does not occur if friction is considerable and the flange splice plate practically does not bend.

Friction coefficient strongly influences the local contact state. Actually, the nonlinear dynamic response is mainly caused by friction between interacting contact surfaces. In general, two types of slipping exist: macro and micro slip. The macro slip occurs when the relative displacement between all of the contact point pairs is similar, that is, no stick regions exist. On the other hand, the micro slip is a transitional process between the macro slip and stick states, where the relative displacements vanish. This transition is not immediate, and the stick and slip areas exist simultaneously during the micro-slipping before the whole contact interface turns into stick. For bolted connections, the stick areas are expected near the bolt shank. Further away, the stick slowly transitions to the slip, and the limit is near the edges of the bolt head or washer. As discussed, the micro- and macro-slipping activations depend on bolt forces and external excitation. With the reduction of the bolt tightening force, the slip region expands until it is active across the whole interface, which activates the macro slip. A case with a strong tightening force and a low excitation force will not result in slipping, as seen in [2]. This corresponds to our previously analyzed case of $\mu > 0.3$.

To get further insight into the contact interaction, let us consider the upper part of the splice connection and the three characteristic contact interfaces: the bolt head/washer, washer/splice plate, and splice plate/flange. The normal contact stress distributions at

these interfaces, before the load release, are given in Fig. 29. The maximum contact

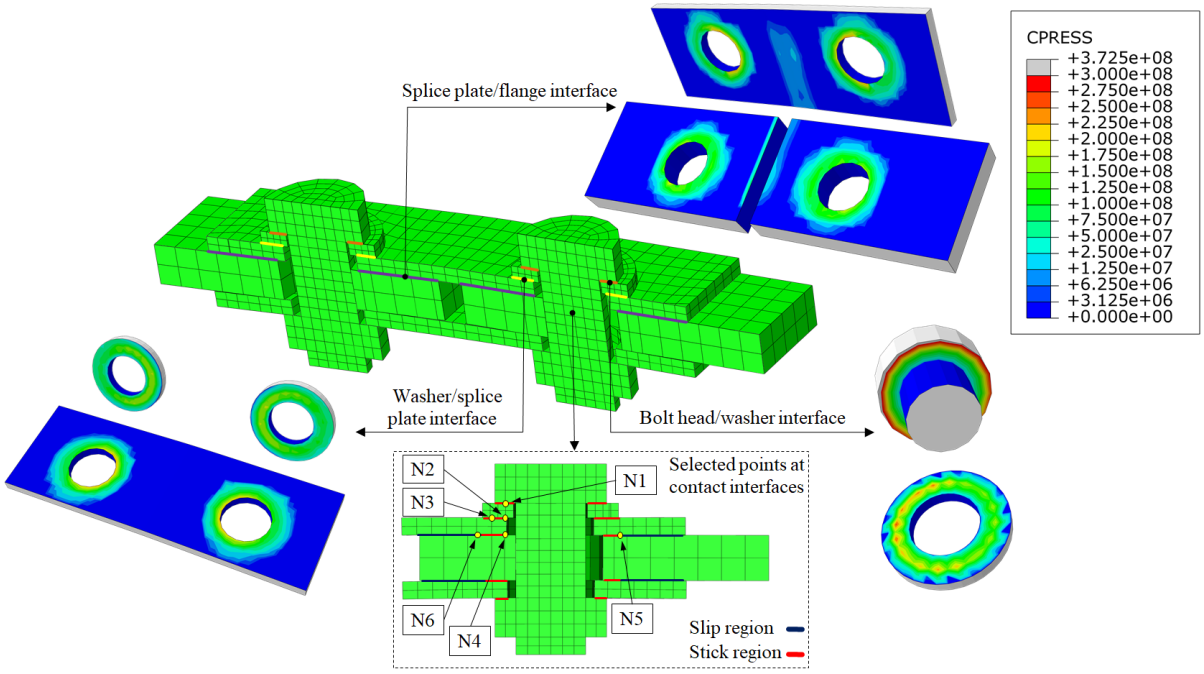

Figure 29: Deformed configuration of the upper part of the splice connection before the load release. The normal contact stress distributions at the contact interfaces: bolt head/washer, washer/splice plate, and splice plate/flange. Six characteristic interacting contact point pairs are designated with N1-N6.

stresses develop around the edges of the bolt holes and bolt heads, and they are concentrated toward the middle of the splice plate. Such a distribution is caused by the bending of the splice plate due to the initial macro-slipping. The maximum contact stress also developed in the middle of the washer due to the stress concentration caused by the bolt head edge.

The deformed configuration in Fig. 29 clearly illustrates that the initial macro slip has occurred at the splice plate/flange interface. In order to scrutinize the slip mechanism inside the bolted connection after the load release, slipping at the selected points is observed. The points N1-N4 are selected near the areas with maximum contact stress, while the points N5 and N6 are defined in the regions with reduced contact stress, symmetrically with respect to the bolt hole, Fig. 29. The slipping between the surfaces at a point is defined as the relative displacement between the two interacting points.

The time history of the relative displacement at point N5 is shown in Fig. 30. Additionally, differences between the two consecutive amplitudes of opposite signs are calculated and plotted for all selected points. These graphs represent the envelopes of the estimated slip amplitudes. It is evident that the relative displacement at point N5 oscillates around the value close to 1.05 mm. This value is the relative static displacement due to the initial macro slip. The first slip amplitude is 43 μm, and it sharply reduces to 11.6 μm in the next cycle. After a few more oscillation cycles, the decay rate reaches a constant value. Similar behavior is obtained for point N6.

After the first two amplitudes, the slip at points N1-N4 is quite similar, although the values at points N1 and N2 are noticeably lower. This is due to the maximum contact

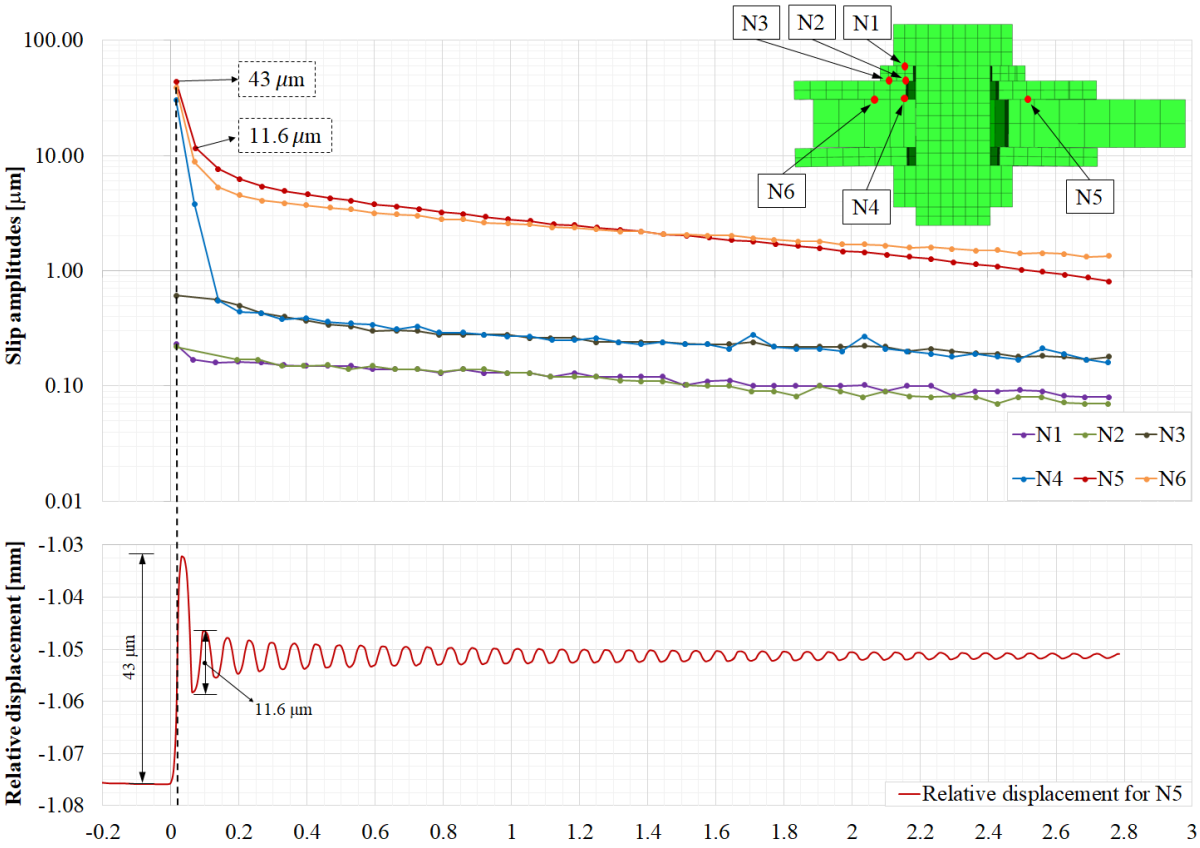

Figure 30: Relative displacement between the characteristic points that are in the contact interaction. Lower figure shows the time history at point N5, while the upper figure gives differences between the consecutive amplitudes of opposite sign for all considered points - slip amplitudes.

stresses that are in the vicinity of points N1 and N2. Nevertheless, the calculated slip amplitudes at points N1-N4 are less than 0.5 μm, which suggests that these points are practically in the stick state.

The slip at point N4 is the most intriguing. This point belongs to the same splice plate/flange contact interface as points N5 and N6. All three points have a similar first amplitude of slip, which suggests the initial uniform displacement between the splice plate and the flange. This behavior can be considered as the macro slip. Between the first and the third amplitudes, the slip value at the point N4 reduces approximately by a factor of 60, and the slip practically vanishes afterwards. On the other hand, the slip amplitudes at points N5 and N6 decay significantly slower. Therefore, the slip at points N5 and N6 monotonically decays, while it abruptly goes to the stick at point N4. The simultaneous presence of the stick and slip zones at the same interface is a clear indicator of the micro slip.

All in all, there are three different types of slipping in our numerical simulation. The first slip takes place during the application of mass M2, when the whole connection slips along the splice plate/flange interface. This represents the initial macro slip and has an approximate amplitude of 1 mm. The second phase occurs immediately after the load release. Again, it consists of the macro-slipping at the splice plate/flange interface, but its amplitude is significantly lower than the initial macro slip, equaling approximately

40 μm. Finally, during the third phase, the stick zone forms at the splice plate/flange interface near the bolt shank, while the slipping is still present further from this region. The existence of stick and slip conditions at the same interface can be considered micro-slipping. As the energy dissipates, the stick region grows steadily until the BBSC becomes practically monolithic. This micro-slipping mechanism is the main cause of nonlinear energy dissipation in mechanical connections.

To summarize, the main conclusions of the presented research are:

- Structural damping is a nonlinear phenomenon that is caused by the complex micro slip state at the contact interfaces of various joints, such as the commonly used bolted beam splice connections. The modeling of structural damping requires a well-designed experimental setup and precise post-processing of the measured data. These are followed by careful calibration, verification, and validation of the numerical model.

- When properly utilized, Abaqus/Explicit is a powerful tool for nonlinear dynamic simulations of structures with bolted connections. The non-physical parameters that require calibration and verification are the FE mesh, mass scaling, spatial and time integration schemes, and contact discretization. To reduce the computational time required, mass scaling is a crucial parameter that must be implemented with particular care.

- Proper calibration of the numerical model with respect to the non-physical parameters allows us to assess the influence of main physical quantities. When the bolt tightening forces are given, one just has to adopt the loading function and the friction coefficient.

- For the adopted numerical model, the friction coefficient is near $\mu = 0.155$, which matches the values reported in the literature. The numerical and experimental results are in excellent correspondence for the case with 100 % of the bolt tightening force, while the agreement of the results slightly deteriorates with the bolt force reduction. Nevertheless, the adopted numerical model predicts nonlinear structural damping with reasonably high accuracy.

- Engineering joints are complex, and their proper detailed numerical modeling is still inefficient for real-life calculations. This fact is the driving force for the development of accurate and efficient models that can provide approximate relations between essential engineering parameters, such as contact stresses, friction, and damping.

As a recommendation for future work, it would be valuable to conduct a similar experiment and to test the mentioned observations regarding the calibration of the numerical model. It is desirable to improve the quality of obtained data by using strain gauges and more accelerometers. The experiment should include a slip-resistant connection with various compositions of high-strength bolts, where influences of the roughness, oxidation, and lubrication would be scrutinized. Furthermore, the position and number of connections and boundary conditions are additional parameters that should be taken into consideration.

Acknowledgments

A. Borković acknowledges the support of the Austrian Science Fund (FWF): M 2806-N.

References

[1] K. L. Johnson. *Contact Mechanics*. Cambridge: Cambridge University Press, 1985. ISBN: 978-0-521-34796-9. DOI: 10.1017/CBO9781139171731.

[2] M. R. W. Brake, ed. *The Mechanics of Jointed Structures: Recent Research and Open Challenges for Developing Predictive Models for Structural Dynamics*. 1st ed. 2018 edition. New York, NY: Springer, July 2017. ISBN: 978-3-319-56816-4.

[3] D. Segalman et al. *Handbook on Dynamics of Jointed Structures*. Tech. rep. July 2009, SAND2009–4164, 1028891. DOI: 10.2172/1028891.

[4] Department for Business, Innovation and Skills. *Airbus in the UK, A400M Wing Assembly at the Manufacturing Facility at Airbus Filton, Bristol*. https://www.flickr.com/photos/bisgovuk/7158201628/. Mar. 2010.

[5] Cblade. *Turbine Blades for Steam Turbine and Gas Turbine Compressor*. https://commons.wikimedia.org/wiki/File:TurbineBlades.jpg. 2009.

[6] L. Pesaresi et al. "Modelling the Nonlinear Behaviour of an Underplatform Damper Test Rig for Turbine Applications". In: *Mechanical Systems and Signal Processing* 85 (Feb. 2017), pp. 662–679. DOI: 10.1016/j.ymssp.2016.09.007.

[7] I. A. Sever, E. P. Petrov, and D. J. Ewins. "Experimental and Numerical Investigation of Rotating Bladed Disk Forced Response Using Underplatform Friction Dampers". In: *Journal of Engineering for Gas Turbines and Power* 130.4 (Apr. 2008). DOI: 10.1115/1.2903845.

[8] H.-T. Thai et al. "Explicit Simulation of Bolted Endplate Composite Beam-to-CFST Column Connections". In: *Thin-Walled Structures* 119 (Oct. 2017), pp. 749–759. DOI: 10.1016/j.tws.2017.07.013.

[9] H. Liu et al. "Mechanical Properties of Bolted Connections for Aluminum Alloy Structures at Elevated Temperatures". In: *Thin-Walled Structures* 157 (Dec. 2020), p. 107067. DOI: 10.1016/j.tws.2020.107067.

[10] K. Jiang, K. H. Tan, and O. Zhao. "Net Section Fracture of S700 High Strength Steel Staggered Bolted Connections". In: *Thin-Walled Structures* 164 (July 2021), p. 107904. DOI: 10.1016/j.tws.2021.107904.

[11] M. Groper. "Microslip and Macroslip in Bolted Joints". In: *Experimental Mechanics* 25.2 (June 1985), pp. 171–174. DOI: 10.1007/BF02328808.

[12] R. N. Hopkins and L. A. A. Heitman. "A Method to Capture Macroslip at Bolted Interfaces". In: *Dynamics of Coupled Structures, Volume 4*. Ed. by M. Allen, R. L. Mayes, and D. Rixen. Conference Proceedings of the Society for Experimental Mechanics Series. Cham: Springer International Publishing, 2016, pp. 213–229. ISBN: 978-3-319-29763-7. DOI: 10.1007/978-3-319-29763-7_21.

[13] L. Gaul and J. Lenz. "Nonlinear Dynamics of Structures Assembled by Bolted Joints". In: *Acta Mechanica* 125.1 (Mar. 1997), pp. 169–181. DOI: 10.1007/BF01177306.

[14] E. Popova and V. L. Popov. "The Research Works of Coulomb and Amontons and Generalized Laws of Friction". In: *Friction* 3.2 (June 2015), pp. 183–190. DOI: 10.1007/s40544-015-0074-6.

[15] M. A. Chowdhury et al. "Sliding Friction of Steel Combinations". In: *The Open Mechanical Engineering Journal* 8.1 (Oct. 2014), pp. 364–369. DOI: 10.2174/1874155X01408010364.

[16] E. Rabinowicz. *Friction and Wear of Materials*. 2nd edition. New York: Wiley-Interscience, July 1995. ISBN: 978-0-471-83084-9.

[17] F. P. Bowden and D. Tabor. *The Friction and Lubrication of Solids*. Revised ed. edition. Oxford : New York: Oxford University Press, Apr. 2001. ISBN: 978-0-19-850777-2.

[18] I. Nitta. "Measurements of Real Contact Areas Using PET Films (Thickness, 0.9 Mm)". In: *Wear*. 10th International Conference on Wear of Materials 181–183 (Mar. 1995), pp. 844–849. DOI: 10.1016/0043-1648(95)90205-8.

[19] V. A. Yastrebov, G. Anciaux, and J.-F. Molinari. "From Infinitesimal to Full Contact between Rough Surfaces: Evolution of the Contact Area". In: *International Journal of Solids and Structures* 52 (Jan. 2015), pp. 83–102. DOI: 10.1016/j.ijsolstr.2014.09.019.

[20] M. Eguchi, T. Shibamiya, and T. Yamamoto. "Measurement of Real Contact Area and Analysis of Stick/Slip Region". In: *Tribology International*. Special Issue: 35th Leeds-Lyon Symposium 42.11 (Dec. 2009), pp. 1781–1791. DOI: 10.1016/j.triboint.2009.04.046.

[21] J. A. Greenwood and J. B. P. Williamson. "Contact of Nominally Flat Surfaces". In: *Proceedings of the Royal Society of London. Series A, Mathematical and Physical Sciences* 295.1442 (1966), pp. 300–319.

[22] J. A. Greenwood, K. L. Johnson, and E. Matsubara. "A Surface Roughness Parameter in Hertz Contact". In: *Wear* 100.1 (Dec. 1984), pp. 47–57. DOI: 10.1016/0043-1648(84)90005-X.

[23] B. N. J. Persson. "Theory of Rubber Friction and Contact Mechanics". In: *The Journal of Chemical Physics* 115.8 (Aug. 2001), pp. 3840–3861. DOI: 10.1063/1.1388626.

[24] P. Wriggers. *Computational Contact Mechanics*. 2nd edition. Berlin ; New York: Springer, May 2006. ISBN: 978-3-540-32608-3.

[25] V. Yastrebov. "Computational Contact Mechanics: Geometry, Detection and Numerical Techniques". In: (Mar. 2011).

[26] S. Bettscheider, C. Gachot, and A. Rosenkranz. "How to Measure the Real Contact Area? A Simple Marker and Relocation Foot-Printing Approach". In: *Tribology International* 103 (Nov. 2016), pp. 167–175. DOI: 10.1016/j.triboint.2016.06.034.

[27] J. F. Archard. "Elastic Deformation and the Laws of Friction". In: *Proceedings of the Royal Society of London. Series A, Mathematical and Physical Sciences* 243.1233 (1957), pp. 190–205.

[28] G. Carbone and F. Bottiglione. "Contact Mechanics of Rough Surfaces: A Comparison between Theories". In: *Meccanica* 46.3 (June 2011), pp. 557–565. DOI: 10.1007/s11012-010-9315-y.

[29] J. R. Barber. "Multiscale Surfaces and Amontons' Law of Friction". In: *Tribology Letters* 49.3 (Mar. 2013), pp. 539–543. DOI: 10.1007/s11249-012-0094-6.

[30] M. H. Müser et al. "Meeting the Contact-Mechanics Challenge". In: *Tribology Letters* 65.4 (Aug. 2017), p. 118. DOI: 10.1007/s11249-017-0900-2.

[31] V. A. Yastrebov et al. "Rough Surface Contact Analysis by Means of the Finite Element Method and of a New Reduced Model". In: *Comptes Rendus Mécanique*. Surface Mechanics : Facts and Numerical Models 339.7 (July 2011), pp. 473–490. DOI: 10.1016/j.crme.2011.05.006.

[32] J. Han et al. "Influence of Metal Forming Parameters on Surface Roughness and Establishment of Surface Roughness Prediction Model". In: *International Journal of Mechanical Sciences* 163 (Nov. 2019). DOI: 10.1016/j.ijmecsci.2019.105093.

[33] A. I. Vakis et al. "Modeling and Simulation in Tribology across Scales: An Overview". In: *Tribology International* 125 (Sept. 2018), pp. 169–199. DOI: 10.1016/j.triboint.2018.02.005.

[34] I. Singer and H. Pollock. *Fundamentals of Friction: Macroscopic and Microscopic Processes*. Vol. 220. Jan. 1992. ISBN: 978-0-7923-1912-2. DOI: 10.1007/978-94-011-2811-7.

[35] M. S. Bonney et al. "Experimental Determination of Frictional Interface Models". In: *Dynamics of Coupled Structures, Volume 4*. Ed. by M. Allen, R. L. Mayes, and D. Rixen. Conference Proceedings of the Society for Experimental Mechanics Series. Cham: Springer International Publishing, 2016, pp. 473–490. ISBN: 978-3-319-29763-7. DOI: 10.1007/978-3-319-29763-7_47.

[36] A. Fantetti et al. "The Impact of Fretting Wear on Structural Dynamics: Experiment and Simulation". In: *Tribology International* 138 (2019), pp. 111–124. DOI: 10.1016/j.triboint.2019.05.023.

[37] P. J. Blau. "Four Great Challenges Confronting Our Understanding and Modeling of Sliding Friction". In: *Tribology Series*. Ed. by D. Dowson et al. Vol. 34. Tribology for Energy Conservation. Elsevier, Jan. 1998, pp. 117–128. DOI: 10.1016/S0167-8922(98)80067-9.

[38] F. P. Bowden and D. Tabor. "Mechanism of Metallic Friction". In: *Nature* 150.3798 (Aug. 1942), pp. 197–199. DOI: 10.1038/150197a0.

[39] M. A. Chowdhury and M. M. Helali. "The Effect of Frequency of Vibration and Humidity on the Coefficient of Friction". In: *Tribology International* 39.9 (Sept. 2006), pp. 958–962. DOI: 10.1016/j.triboint.2005.10.002.

[40] W. Y. H. Liew. "Effect of Relative Humidity on the Unlubricated Wear of Metals". In: *Wear* 260.7 (Apr. 2006), pp. 720–727. DOI: 10.1016/j.wear.2005.04.011.

[41] P. J. Blau. *Friction Science and Technology: From Concepts to Applications, Second Edition*. Second. Boca Raton: CRC Press, Oct. 2008. ISBN: 978-0-429-13711-2. DOI: 10.1201/9781420054101.

[42] D. Tabor. "Friction—The Present State of Our Understanding". In: *Journal of Lubrication Technology* 103.2 (Apr. 1981), pp. 169–179. DOI: 10.1115/1.3251622.

[43] M. D. Pashley, J. B. Pethica, and D. Tabor. "Adhesion and Micromechanical Properties of Metal Surfaces". In: *Wear* 100.1 (Dec. 1984), pp. 7–31. DOI: 10.1016/0043-1648(84)90003-6.

[44] J. S. McFarlane, D. Tabor, and F. P. Bowden. "Relation between Friction and Adhesion". In: *Proceedings of the Royal Society of London. Series A. Mathematical and Physical Sciences* 202.1069 (July 1950), pp. 244–253. DOI: 10.1098/rspa.1950.0097.

[45] G. W. Stachowiak and A. W. Batchelor. *Engineering Tribology*. 3rd edition. Amsterdam ; Boston: Butterworth-Heinemann, Sept. 2005. ISBN: 978-0-7506-7836-0.

[46] S. Venkatesan and D. A. Rigney. "Sliding Friction and Wear of Plain Carbon Steels in Air and Vacuum". In: *Wear* 153.1 (Mar. 1992), pp. 163–178. DOI: 10.1016/0043-1648(92)90268-D.

[47] F. P. Bowden and G. W. Rowe. "The Adhesion of Clean Metals". In: *Proceedings of the Royal Society of London. Series A. Mathematical and Physical Sciences* 233.1195 (Jan. 1956), pp. 429–442. DOI: 10.1098/rspa.1956.0001.

[48] P. L. Menezes et al. *Tribology for Scientists and Engineers: From Basics to Advanced Concepts*. Springer Science & Business Media, Dec. 2013. ISBN: 978-1-4614-1945-7.

[49] M. J. Furey. "Surface Temperatures in Sliding Contact". In: *A S L E Transactions* 7.2 (Jan. 1964), pp. 133–146. DOI: 10.1080/05698196408972043.

[50] Y. Waddad et al. "Heat Partition and Surface Temperature in Sliding Contact Systems of Rough Surfaces". In: *International Journal of Heat and Mass Transfer* 137 (July 2019), pp. 1167–1182. DOI: 10.1016/j.ijheatmasstransfer.2019.04.015.

[51] W. Qin et al. "Effects of Surface Roughness on Local Friction and Temperature Distributions in a Steel-on-Steel Fretting Contact". In: *Tribology International* 120 (Apr. 2018), pp. 350–357. DOI: 10.1016/j.triboint.2018.01.016.

[52] C. W. Schwingshackl, E. P. Petrov, and D. J. Ewins. "Measured and Estimated Friction Interface Parameters in a Nonlinear Dynamic Analysis". In: *Mechanical Systems and Signal Processing*. Interdisciplinary and Integration Aspects in Structural Health Monitoring 28 (Apr. 2012), pp. 574–584. DOI: 10.1016/j.ymssp.2011.10.005.

[53] D. L. Goldsby and T. E. Tullis. "Flash Heating Leads to Low Frictional Strength of Crustal Rocks at Earthquake Slip Rates". In: *Science* 334.6053 (Oct. 2011), pp. 216–218. DOI: 10.1126/science.1207902.

[54] H. R. Le, M. P. F. Sutcliffe, and J. A. Williams. "Friction and Material Transfer in Micro-Scale Sliding Contact between Aluminium Alloy and Steel". In: *Tribology Letters* 18.1 (Jan. 2005), pp. 99–104. DOI: 10.1007/s11249-004-1762-y.

[55] S. Rohm et al. “Friction Between Steel and Snow in Dependence of the Steel Roughness”. In: *Tribology Letters* 59.1 (June 2015), p. 27. DOI: 10.1007/s11249-015-0554-x.

[56] Y. Meng et al. “A Review of Recent Advances in Tribology”. In: *Friction* 8.2 (Apr. 2020), pp. 221–300. DOI: 10.1007/s40544-020-0367-2.

[57] T. Mang, ed. *Encyclopedia of Lubricants and Lubrication*. 2014th edition. New York: Springer, Jan. 2014. ISBN: 978-3-642-22646-5.

[58] C. V. Madhusudana. *Thermal Contact Conductance*. Mechanical Engineering Series. Cham: Springer International Publishing, 2014. ISBN: 978-3-319-01275-9. DOI: 10.1007/978-3-319-01276-6.

[59] B. N. J. Persson and E. Tosatti, eds. *Physics of Sliding Friction*. 1996th edition. Dordrecht ; Boston: Springer, Feb. 1996. ISBN: 978-0-7923-3935-9.

[60] E. E. Ungar. *Energy Dissipation at Structural Joints; Mechanisms and Magnitudes*. Tech. rep. AD0607257. Aug. 1964. Chap. Technical Reports.

[61] E. E. Ungar. “The Status of Engineering Knowledge Concerning the Damping of Built-up Structures”. In: *Journal of Sound and Vibration* 26.1 (Jan. 1973), pp. 141–154. DOI: 10.1016/S0022-460X(73)80210-X.

[62] C. Hartwigsen et al. “Experimental Study of Non-Linear Effects in a Typical Shear Lap Joint Configuration”. In: *Journal of Sound and Vibration* 277.1-2 (Oct. 2004), pp. 327–351. DOI: 10.1016/j.jsv.2003.09.018.

[63] H. G. D. Goyder et al. “Friction and Damping Associated with Bolted Joints: Results and Signal Processing”. In: *Proceedings of the ISMA 2016 International Conference on Noise and Vibration Engineering, Leuven*. 2016, p. 11.

[64] L. Gaul and R. Nitsche. “The Role of Friction in Mechanical Joints”. In: *Applied Mechanics Reviews* 54.2 (Mar. 2001), pp. 93–106. DOI: 10.1115/1.3097294.

[65] C. Li et al. “Modeling Method of Bolted Joints with Micro-Slip Features and Its Application in Flanged Cylindrical Shell”. In: *Thin-Walled Structures* 164 (July 2021), p. 107854. DOI: 10.1016/j.tws.2021.107854.

[66] D. Segalman. *An Initial Overview of Iwan Modeling for Mechanical Joints*. Tech. rep. SAND2001-0811, 780307. Mar. 2001. DOI: 10.2172/780307.

[67] W. D. Iwan. “On a Class of Models for the Yielding Behavior of Continuous and Composite Systems”. In: *Journal of Applied Mechanics* 34.3 (Sept. 1967), pp. 612–617. DOI: 10.1115/1.3607751.

[68] D. J. Segalman. “A Four-Parameter Iwan Model for Lap-Type Joints”. In: *Journal of Applied Mechanics* 72.5 (Feb. 2005), pp. 752–760. DOI: 10.1115/1.1989354.

[69] B. J. Deaner et al. “Investigation of Modal Iwan Models for Structures with Bolted Joints”. In: *Topics in Experimental Dynamic Substructuring, Volume 2*. Ed. by R. Mayes, D. Rixen, and M. Allen. Conference Proceedings of the Society for Experimental Mechanics Series. New York, NY: Springer, 2014, pp. 9–25. ISBN: 978-1-4614-6540-9. DOI: 10.1007/978-1-4614-6540-9_2.

[70] D. Roettgen et al. “Substructuring of a Nonlinear Beam Using a Modal Iwan Framework, Part I: Nonlinear Modal Model Identification”. In: *Dynamics of Coupled Structures, Volume 4*. Ed. by M. S. Allen, R. L. Mayes, and D. J. Rixen. Conference Proceedings of the Society for Experimental Mechanics Series. Cham: Springer International Publishing, 2017, pp. 165–178. ISBN: 978-3-319-54930-9. DOI: 10.1007/978-3-319-54930-9_15.

[71] J. R. Barber. *Contact Mechanics*. Springer, Feb. 2018. ISBN: 978-3-319-70939-0.

[72] A. Konyukhov and R. Izi. *Introduction to Computational Contact Mechanics: A Geometrical Approach*. 1st edition. Chichester, West Sussex: Wiley, June 2015. ISBN: 978-1-118-77065-8.

[73] O. Mijatović et al. “Experimental Analysis of Structural Damping for Bolted and Welded Splice Connection Joint for IPE-80 Steel Profile”. In: *International conference on Contemporary Theory and Practice in Construction* 14 (June 2020). DOI: 10.7251/STP2014032M.

[74] O. Mijatović et al. “Numerical and Experimental Anaysis of Structural Damping for Bolted Splice Connection Joint”. In: *Journal of Faculty of Civil Engineering* 37 (2021), pp. 297–307. DOI: 10.14415/konferencijaGFS2021.28.

[75] L. Carlotta Pagnini and G. Solari. “Damping Measurements of Steel Poles and Tubular Towers”. In: *Engineering Structures* 23.9 (Sept. 2001), pp. 1085–1095. DOI: 10.1016/S0141-0296(01)00011-6.

[76] M. C. Moynihan and J. M. Allwood. “Utilization of Structural Steel in Buildings”. In: *Proceedings of the Royal Society A: Mathematical, Physical and Engineering Sciences* 470.2168 (Aug. 2014), p. 20140170. DOI: 10.1098/rspa.2014.0170.

[77] C. F. Dunant et al. “Regularity and Optimisation Practice in Steel Structural Frames in Real Design Cases”. In: *Resources, Conservation and Recycling* 134 (July 2018), pp. 294–302. DOI: 10.1016/j.resconrec.2018.01.009.

[78] J.-P. Jaspart and K. Weynand. *Design of Joints in Steel Structures: Eurocode 3: Design of Steel Structures; Part 1-8 Design of Joints*. 1st edition. Ernst & Sohn, June 2017. ISBN: 978-3-433-60871-5.

[79] I. Vayas, J. Ermopoulos, and G. Ioannidis. *Design of Steel Structures to Eurocodes*. Springer International Publishing, Dec. 2018. ISBN: 978-3-319-95473-8.

[80] F. Magalhães et al. “Damping Estimation Using Free Decays and Ambient Vibration Tests”. In: *Mechanical Systems and Signal Processing*. Special Issue: Operational Modal Analysis 24.5 (July 2010), pp. 1274–1290. DOI: 10.1016/j.ymssp.2009.02.011.

[81] P. Avitabile. *Modal Testing: A Practitioner’s Guide*. 1st edition. Hoboken, NJ: Wiley, Nov. 2017. ISBN: 978-1-119-22289-7.

[82] R. Brincker, C. E. Ventura, and P. Andersen. “Damping Estimation by Frequency Domain Decomposition”. In: *Proceedings of IMAC 19* (2001), pp. 698–703.

[83] A. Cunha, E. Caetano, and R. Delgado. “Dynamic Tests on Large Cable-Stayed Bridge”. In: *Journal of Bridge Engineering* 6.1 (Feb. 2001), pp. 54–62. DOI: 10.1061/(ASCE)1084-0702(2001)6:1(54).

[84] T. Diehl, D. Carroll, and B. Nagaraj. "Applications of DSP to Explicit Dynamic FEA Simulations of Elastically-Dominated Impact Problems". In: *Shock and Vibration* 7.3 (2000), pp. 167–177. DOI: 10.1155/2000/931351.

[85] T. S. Edwards. "Effects of Aliasing on Numerical Integration". In: *Mechanical Systems and Signal Processing* 21.1 (Jan. 2007), pp. 165–176. DOI: 10.1016/j.ymssp.2005.08.009.

[86] *Getting Started with ABAQUS/Explicit: Keywords Version (v6.5-1).* https://classes.engineering.wustl.edu/2009/spring/mase5513/abaqus/docs/v6.5.

[87] L. Fasanella and K. E. Jackson. *Best Practices for Crash Modeling and Simulation.* Tech. rep. NASA/TM-2002-211944. 2002, p. 99.

[88] *ABAQUS. User's Manual, Version 6.14.* Dassault Systemes Corp., Providence, RI, USA, 2014.

[89] R. J. Boulbes. *Troubleshooting Finite-Element Modeling with Abaqus: With Application in Structural Engineering Analysis.* 1st ed. 2020 edition. Cham: Springer, Sept. 2019. ISBN: 978-3-030-26739-1.

[90] R. Stafford. *Cumulative Cubic Integration , MATLAB Central File Exchange.* https://www.mathworks.com/matlabcentral/fileexchange/19152-cumulative-cubic-integration. Retrieved August 29, 2022.

[91] H. Goyder, P. Ind, and D. Brown. *Development of a Method for Measuring Damping in Bolted Joints.* Jan. 2011. DOI: 10.1115/DETC2011-47230.

[92] H. Goyder, P. Ind, and D. Brown. "Measurement of Damping in Bolted Joints". In: *ASME 2012 International Design Engineering Technical Conferences and Computers and Information in Engineering Conference.* American Society of Mechanical Engineers Digital Collection, Sept. 2013, pp. 399–408. DOI: 10.1115/DETC2012-70896.

[93] *Optimization Toolbox User's Guide, R2016b, 2016.* The MathWorks, Inc. 3 Apple Hill Drive Natick, MA 01760-2098.

[94] Z. Ugray et al. "Scatter Search and Local NLP Solvers: A Multistart Framework for Global Optimization". In: *INFORMS Journal on Computing* 19.3 (Aug. 2007), pp. 328–340. DOI: 10.1287/ijoc.1060.0175.

[95] G. Dinger and C. Friedrich. "Avoiding Self-Loosening Failure of Bolted Joints with Numerical Assessment of Local Contact State". In: *Engineering Failure Analysis* 18.8 (Dec. 2011), pp. 2188–2200. DOI: 10.1016/j.engfailanal.2011.07.012.

[96] W. Chen and X. Deng. "Structural Damping Caused by Micro-Slip along Frictional Interfaces". In: *International Journal of Mechanical Sciences* 47.8 (2005), pp. 1191–1211. DOI: 10.1016/j.ijmecsci.2005.04.005.

[97] H. Wentzel and M. Olsson. "Mechanisms of Dissipation in Frictional Joints - Influence of Sharp Contact Edges and Plastic Deformation". In: *Wear* 265.11 (Nov. 2008), pp. 1814–1819. DOI: 10.1016/j.wear.2008.04.026.

[98] M. Pavlović et al. "Friction Connection vs. Ring Flange Connection in Steel Towers for Wind Converters". In: *Engineering Structures* 98 (Sept. 2015), pp. 151–162. DOI: 10.1016/j.engstruct.2015.04.026.

[99] B. Egan et al. “Modelling a Single-Bolt Countersunk Composite Joint Using Implicit and Explicit Finite Element Analysis”. In: *Computational Materials Science*. Proceedings of the 21st International Workshop on Computational Mechanics of Materials (IWCMM 21) 64 (Nov. 2012), pp. 203–208. DOI: 10.1016/j.commatsci.2012.02.008.

[100] M. A. McCarthy et al. “Three-Dimensional Finite Element Analysis of Single-Bolt, Single-Lap Composite Bolted Joints: Part I—Model Development and Validation”. In: *Composite Structures* 71.2 (Nov. 2005), pp. 140–158. DOI: 10.1016/j.compstruct.2004.09.024.

[101] J. VonNeumann and R. D. Richtmyer. “A Method for the Numerical Calculation of Hydrodynamic Shocks”. In: *Journal of Applied Physics* 21.3 (Mar. 1950), pp. 232–237. DOI: 10.1063/1.1699639.

[102] L. Mahéo, V. Grolleau, and G. Rio. “Numerical Damping of Spurious Oscillations: A Comparison between the Bulk Viscosity Method and the Explicit Dissipative Tchamwa-Wielgosz Scheme”. In: *Computational Mechanics* 51.1 (2013), pp. 109–128. DOI: 10.1007/s00466-012-0708-8.

[103] T. Belytschko et al. “Hourglass Control in Linear and Nonlinear Problems”. In: *Computer Methods in Applied Mechanics and Engineering* 43.3 (May 1984), pp. 251–276. DOI: 10.1016/0045-7825(84)90067-7.

[104] D. P. Flanagan and T. Belytschko. “A Uniform Strain Hexahedron and Quadrilateral with Orthogonal Hourglass Control”. In: *International Journal for Numerical Methods in Engineering* 17.5 (1981), pp. 679–706. DOI: 10.1002/nme.1620170504.

[105] *I. LSTC, G. DYNAmore, Total Energy, LS-DYNA Support. (2022).* http://www.dynasupport.com/howtos/general/total-energy (accessed August 29, 2022).

[106] G. Zheng et al. “Dynamic Analysis of Lunar Lander during Soft Landing Using Explicit Finite Element Method”. In: *Acta Astronautica* 148 (July 2018), pp. 69–81. DOI: 10.1016/j.actaastro.2018.04.014.

[107] Z.-H. Zhong. *Finite Element Procedures for Contact-Impact Problems*. Oxford, New York: Oxford University Press, June 1993. ISBN: 978-0-19-856383-9.

[108] N. Jakšić and K.-F. Nilsson. “Numerical Simulation of One Metre Drop Test on Bar for CASTOR Cask”. In: *Packaging, Transport, Storage & Security of Radioactive Material* 19.3 (Sept. 2008), pp. 142–150. DOI: 10.1179/174651008X344430.